ASCE

Characterization of Textile-Reinforced Mortar: State of the Art and Detail-Level Modeling with a Free Open-Source Finite-Element Code

Ingrid Boem, Ph.D.

Abstract: The research addressed in the paper is aimed at calibrating a numerical model developed by using a free open-source finite-element code for the assessment of the structural performances of historical masonry buildings strengthened using the textile-reinforced mortar (TRM) technique. TRM is a near-surface-mounted system, which couples inorganic matrices with fiber-based textile or meshes. The main purpose is to develop a multiple-level numerical approach, starting with the detailed modeling of components and interfaces, followed by a computationally efficient intermediate level model, using layered elements, for the calibration of a lumped plasticity-based model suitable for the global analysis of structures. In this paper, the first research results are presented. In particular, a broad literature review concerning the mechanical characterization and analysis of TRM systems is collected. Then, the calibration of the numerical model, the validation through comparison with the results of experimental characterization tests available in the literature (tensile, shear bond, and in-plane shear tests) and a sensitivity analysis are reported. Nonlinear static analyses were performed, considering the nonlinearity of the composite material components and interfaces. The model was capable of accounting for the main parameters affecting the behavior of the composite material, such as the reinforcement ratio and orientation, the mortar characteristics and the wire–mortar interaction and proved to be a valid tool to investigate the optimization of TRM applicative details. **DOI:** [10.1061/(ASCE)CC.1943-5614.0001240](#). *This work is made available under the terms of the Creative Commons Attribution 4.0 International license, https://creativecommons.org/licenses/by/4.0/.*

Author keywords: Seismic vulnerability; Masonry strengthening; Composites; TRM; CRM; Numerical modeling; OOFEM.

Introduction

Masonry, composed of brick or stone units jointed through weak lime mortar, represents the par excellence and most widespread construction material for historical buildings, characterizing many urban and rural centers, often part of the architectural and cultural heritage (Fernandes et al. 2010). Unfortunately, these structures are particularly vulnerable to exceptional actions (earthquakes, crushing, blasts) and to long-term materials deterioration (Binda et al. 2003; Makovička and Makovička 2003; Gostič and Dolinšek 2008; Ural et al. 2012; Basset-Salom and Guardiola-Víllora 2014; Penna et al. 2014; Fiorentino et al. 2018; Sorrentino et al. 2019; Wilson et al. 2017). Thus, to ensure safety and conservation of these assets, structural interventions are often needed (Tomaževič 1999) to provide an effective connection between floors and walls and between adjacent walls, to counteract pushing elements, to prevent the masonry disaggregation or multiple-leaf separation phenomena. In addition, it is sometimes necessary to increase the masonry resistance itself (in-plane and/or out-of-plane).

For this purpose, the application of textile-reinforced mortars (TRMs) represents an innovative, effective, and compatible reinforcement strategy, consisting of plastering the masonry walls by means of mortars with fiber-based elements embedded (meshes or textiles made of long fibers, made for example of carbon, glass, basalt). In the literature, TRM are also called fiber-reinforced cementitious matrix/mortar (FRCM), textile-reinforced concrete (TRC), TRM, fabric-reinforced mortar (FRM), or inorganic matrix-grid (IMG) composites. Such types of reinforcement avoid the typical durability drawbacks related to ordinary steel corrosion; moreover, the application of inorganic matrix fosters compatibility with the masonry substrate, transpirability, fire resistance, easiness of application, and reversibility (Papanicolaou et al. 2007a, b). Over the last 20 years, many researchers focused on the development of TRM systems and on the experimental evaluation of the performances of TRM-strengthened masonry elements (Kouris and Triantafillou 2018). Although some codes and guidelines have already been released (ACI 2016; CSLP 2018, 2019a, b; ACI 2020; CNR 2020), the definition of a broad, structured predictive model for TRM-strengthened masonry is still a current issue. The robust computational models developed for unreinforced masonry (Lourenço and Rots 1997; Magenes 2000; Calderini and Lagomarsino 2008; Macorini and Izzuddin 2013) cannot be adopted as-are for TRM applications, due to the complex interactions with the masonry substrate and within the reinforcement.

In this context, the project "conFiRMa" (Boem 2021a), acronym for "calibration of a numerical model for fiber-reinforced mortar analysis," is aimed at calibrating a validated numerical method, implemented using a free, open-source finite-element code (Patzák and Bittnar 2001; Patzák 2002, 2012) for the assessment of the structural performances of historical masonry buildings strengthened with TRM. The purpose is to develop a multiple-level approach, starting with the detailed modeling of components and mutual interfaces, followed by an optimization procedure to get a computationally efficient intermediate level model (e.g., using layered elements) for the calibration of the lumped plasticity-based model suitable for the global analysis of structures. This paper

Research Fellow, Dept. of Concrete and Masonry Structures, Faculty of Civil Engineering, Czech Technical Univ., Thákurova 7, 166 29 Praha 6, Czech Republic. ORCID: https://orcid.org/0000-0003-3646-0642. Email: ingrid.boem@fsv.cvut.cz
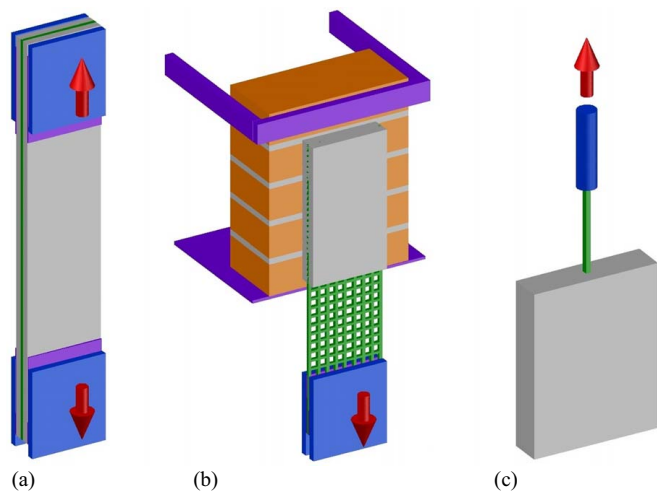
Fig. 1. Characterization tests for TRM: (a) direct tensile tests; (b) shear bond tests; and (c) pullout tests.

deals with the characterization of the TRM systems: a broad literature review is initially presented, giving a wide overview on experimental, analytical, and numerical aspects. Then, the results concerning the selection, calibration, and validation of the TRM material model at the detailed level are presented. In particular, nonlinear static analyses are performed, considering the nonlinearity of the material components and interfaces. The results of previous experimental tests available in the literature, concerning TRM mechanical characterization, are considered: in particular, pullout tests, to calibrate the interaction between the mortar matrix and the embedded reinforcement; and tensile tests, shear bond tests, and in-plane shear tests, to validate the numerical model. Moreover, a sensitivity analysis allows to investigate on the main parameters influencing the response.

State of the Art

A number of experimental tests performed in the last 10–15 years for the characterization of different TRM systems is available in the literature; in addition, analytic and numeric models were developed and calibrated, to deeply analyze the resisting mechanisms and provide robust interpretations. This literature review is aimed at depicting the great variety of aspects that deserve attention when dealing with TRMs characterization, related to the multitude of possible materials combinations as well as to their mutual interaction and with the masonry support.

Experimental Evidences

The experimental characterization tests on TRMs typically concern tensile tests on TRM coupons [Fig. 1(a)] and shear–bond tests on TRM layers applied on masonry substrates [Fig. 1(b)]. The most relevant results are related to the activities of the RILEM Technical Committee 250-CSM (2012–2019), which involved different European research institutions focusing on the study of synthetic and inorganic fibers (Caggegi et al. 2017; Carozzi et al. 2017; De Santis et al. 2017a; Leone et al. 2017; Lignola et al. 2017). In addition, some attention was devoted to the use of natural fibers, which can represent a more sustainable and optimized alternative (Olivito et al. 2016; de Carvalho Bello et al. 2019; Trochoutsou et al. 2021).

In the tensile tests, the TRM layer is gripped at opposite ends and pulled according to monotonic loading, allowing the

measurement of the equivalent stress–strain behavior of the composite material. The response is generally characterized by a tri-phase curve, consisting in a first elastic branch (as the mortar remains uncracked), a second cracking-formation stage (with cracks approximately orthogonal to the loading direction), and a final crack-stabilization branch (De Santis et al. 2017b). In the latter, the stiffness is almost comparable with that of the bare textile and possible tension-stiffening effect due to the mortar within the cracks that may occur, but the stiffness can sometimes be lower, due to the telescopic failure of the yarns (Larrinaga et al. 2014). The extent of each stage depends on the characteristics of the combined materials and their mutual interaction. The strains in the textile rise suddenly once a crack forms, just in correspondence of the fracture (Liu et al. 2021; Trochoutsou et al. 2021); as the load increase, new cracks form, inducing other localized strain peaks in the textile. When the tensile stress in the intact mortar between cracks can no longer increase, the cracks stabilize (the minimum crack distance is reached). Typically, more and closer cracks result by using properly coated or pre-impregnated textiles, in respect to dry reinforcements, since the bond performances with the mortar matrix are improved; similarly, under a constant reinforcement ratio, the use of closer grid sizes, within certain limits, can led to a more diffuse crack pattern. The coating can also improve the ultimate tensile strength and stiffness in the cracked stage; more resistant mortars can result in closer cracks, which typically develop at the location of the transversal yarns.

The collapse may be induced by the textile failure or by the textile slippage in the gripping area; spalling of the mortar may also occur. Several authors warned about the importance of an adequate design of the clamping heads when testing TRMs, since unrealistic stress concentration, local damage, or slippage may distort the global response of the samples (De Santis and de Felice 2015; Arboleda et al. 2016; D'Antino and Papanicolaou 2018; Kim et al. 2018).

In shear–bond tests, the TRM layer is applied on a masonry substrate and loaded in parallel to that surface, by applying a shear tearing to the textile (single- or double-lap shear tests); a proper setup adjustment is necessary to limit eccentricity and/or misalignment (Calabrese et al. 2020). The results are generally reported in terms of textile stresses at the varying of the textile slip; the collapse may occur for debonding of the TRM layer from the masonry substrate or at the textile–mortar interface; in addition, slippage of the textile within the matrix or textile failure can arise. Usually, for lower force values, the strains in the textile activates in the vicinity to the loaded side; then, for higher force values, the involved length increases (D'Antino et al. 2014). By testing different bond lengths (de Felice et al. 2014; Carozzi and Poggi 2015; Alecci et al. 2016; Askouni and Papanicolaou 2017; Donnini and Corinaldesi 2017; Gattesco and Boem 2017a; Rovero et al. 2020, Hadad et al. 2021), it is possible to check for the minimum anchorage; it is also possible to calibrate the local bond–slip relationship between the textile and the matrix, useful for numerical simulations (D'Ambrisi et al. 2013; Santandrea et al. 2020). Although the debonding from the substrate is not a common failure mode in TRM systems, the type of masonry may influence the effectiveness of the TRM application (de Felice et al. 2014; De Santis and de Felice 2015; Bilotta et al. 2017; Senaldi et al. 2020) and the mortar deterioration tends to reduce the bond capability (Grande et al. 2013). However, the surface preparation (cleaning from dust, adequate roughness, sandblasting, wetting, curing procedure) can significantly improve the bond (Razavizadeh et al. 2014; De Santis and de Felice 2015).

The characterization tests obtain the design parameters for TRM reinforcements (Ascione et al. 2015). The bond between the textile

and the matrix is confirmed as fundamental in determining the performances of TRM systems, which can be improved by the coating (Dvorkin et al. 2013; Donnini et al. 2016; D'Antino and Papanicolaou 2017) as well as by surface treatments (Martins et al. 2015; Donnini et al. 2016; D'Antino and Papanicolaou 2017; Signorini, et al. 2018a) or a proper textile configuration (Peled and Bentur 2003; Padalu et al. 2018; Askouni and Papanicolaou 2019). To better investigate of this key aspect, that is, the yarn-to-matrix interaction, some authors performed pullout experimental tests on single yarns or small portions of textile [Fig. 1(c)], to calibrate the fiber-to-mortar slip response (Dvorkin et al. 2013; Ghiassi et al. 2016; Gattesco and Boem 2017a; Dalalbashi et al. 2018a). The typical pullout behavior of unribbed rods emerged (Cosenza et al. 1997): the shear–bond performances are characterized by an initial elastic branch, followed by a progressive stiffness degradation, as chemical adhesion is lost and debonding develops, and a descending branch, mostly governed by the friction due to the interface surface roughness, which mostly depends on the coating treatment rather than the matrix characteristics (Contamine et al. 2011; Zhu et al. 2011; Carozzi and Poggi 2015; Martins et al. 2015; Bellini and Mazzotti 2016; Dalalbashi et al. 2018b; Donnini et al. 2018; Bellini et al. 2019; Liu et al. 2019). Benefits were recognized in multiple-ply configurations, with the formation of more cracks, as the number of ply increased (Larrinaga et al. 2014; Bilotta et al. 2017; Liu et al. 2021); however, the improvement resulted often less-than-proportional, as the matrix delamination occurred (Donnini and Corinaldesi 2017; Calabrese et al. 2020).

Some authors also analyzed the influence of the load cyclicity and load rate on the TRM characterization tests. Tensile and shear–bond cyclic tests revealed performances quite comparable with that of monotonic loading, in terms of strength, but some more pronounced displacements, when the progressive deterioration of the textile–matrix interface during cycles occurred (Carozzi and Poggi 2015; Bellini and Mazzotti 2016; Bellini et al. 2019); this emphasized delamination can also led to wider and more spaced cracks (De Santis and de Felice 2015). Quasi-static monotonic loading resulted as a safe-side approach in respect to high-speed loading and provided generally comparable or even lower performances (Zhu et al. 2011; Liu et al. 2019). Few experimental outcomes are available on the in-plane shear response of TRM layers; however, some picture-frame shear tests were performed by applying monotonic diagonal compression (Contamine et al. 2011) or horizontal cyclic loading (Sisti et al. 2019). The tests evidenced an appreciable global ductility, due to the presence of the embedded reinforcement crossing the mortar cracks, which allowed a wide crack diffusion.

TRM systems can be exposed to harsh environmental conditions, such as saline air or water, high temperatures, wet–dry or freeze–thaw cycles, and salt migration from the subsoil (Al-Lami et al. 2020); moreover, the alkaline ions content of the inorganic matrix itself can be detrimental. Accelerating aging protocols, based on baths in specific solutions under controlled temperature, are typically performed to investigate TRM durability. However, the correlation between the accelerated tests and natural conditions is still going to be determined (see, for example, the activities of the RILEM Technical Committee 290-IMC, started in 2019).

Tensile tests on bare fiber-based textiles evidenced a higher sensitivity to alkaline baths of E-glass and basalt dry fibers, in respect to alkali resistant (AR) glass and PBO, while carbon fibers were very limitedly influenced (Micelli and Aiello 2019). The pre-impregnation of AR-glass fibers with polymeric resin provided an effective protection against deterioration; fatigue loading treatments enhanced degradation in strength and Young's modulus (Righetti et al. 2016; Micelli et al. 2017).

Tests on TRM made of pre-impregnated AR glass evidenced that that alkaline and saline environments can induce the premature textile slippage from the mortar matrix, resulting in both decreases of the ultimate tensile strength and strain capacities (Butler et al. 2009, 2010; Nobili 2016). Wetting and dry cycles favored the saline penetration, reducing the bond between the TRM layer and the masonry substrate (Donnini 2019). TRM systems based on dry PBO textiles were analyzed by Senaldi et al. (2020) and Arboleda et al. (2014): moist, saline, alkaline, water, and freeze–thaw conditions revealed only in some cases a moderate decrease in the ultimate tensile strength and strain, related to the deterioration of the textile and/or its bond. Nobili and Signorini (2017) and Signorini et al. (2018b) found, for impregnated carbon TRM, that saline and alkaline environments are especially detrimental for the textile–matrix bond, evidencing in the tensile tests a reduced number of wider cracks; however, early-stage protection limits this effect. Distilled water, hydrochloric acid, and freeze–thaw cycles had a lesser impact on the performances. Tran et al. (2019) evidenced that the lap–splice performances of carbon textiles can be affected by harsh conditions (saline, high temperature, humidity, sustained load). High temperatures affected the textile bonding, due to modifications in the organic resins used for impregnation (Liu et al. 2019; Silva et al. 2014; however, within certain temperature limits (≤200°C), TRM preheated and then tested at room temperature showed just small alterations (Colombo et al. 2011; Donnini et al. 2017).

Analytical Procedures

For the description of the textile–matrix slip phenomena, the researchers generally assumed pure Mode-II fracture mechanics and provided the cohesive material law representing the shear stress at the interface at the varying of the relative slip between the textile and the matrix, along the longitudinal direction. Both pullout and shear–bond experimental characterization tests served for the calibration. Shear stress–slip laws were based either on simplified bilinear/trilinear functions (Carozzi et al. 2016; Olivito et al. 2016; D'Antino et al. 2018; Calabrese et al. 2019; Colombi and D'Antino 2019; Barducci et al. 2020; Rovero et al. 2020) or on more articulated nonlinear functions (D'Ambrisi et al. 2013; Carozzi et al. 2014; Focacci et al. 2017; Dalalbashi et al. 2018b; Ascione et al. 2020; Santandrea et al. 2020). The residual shear stress was tended to zero or to a constant value related to friction at the debonded interface. Once the stress–slip law was defined, the global load–slip behavior of the TRM strip subjected to bond test was evaluated by setting a system of differential equations along the bonded length, based on displacement compatibility and force equilibrium. Grande et al. (2018) adopted a simplified elastic/brittle relationship for the shear stress–slip but also introduced the possibility of tensile failure for the mortar.

In regard to the direct tensile tests, Focacci et al. (2020) analyzed analytically the local behavior of TRM samples assuming nonlinear functions for both the fiber–matrix interface and the matrix and provided the TRM tensile stress–strain analytical curve by solving a system of differential equations. Similarly, Grande et al. (2020) proposed a theoretical model, based on equilibrium considerations and differential equations, able to predict the crack pattern of TRM elements subjected to tension, considering the nonlinear local behavior of the matrix, the reinforcement, and the reinforcement/matrix interface. This method was capable to predict each single crack formation; differently, other authors focused on the prediction the TRM equivalent tensile tri-linear behavior. For example, Larrinaga et al. (2014) and Liu et al. (2021) applied the Aveston–Cooper–Kelly theory (Aveston and Kelly 1973). Liu et al. (2021) also compared the

results of the Aveston–Cooper–Kelly model with those obtained from the Comité Euro-International du Béton (CEB) model (CEB 2010) for reinforcement concrete cracking considering the tension–stiffening effect. Larrinaga et al. (2013) proposed the "cracking model," based on the Eurocode 2 approach for concrete crack control (CEN 2004) and assumed a nonlinear relationship for the textile accounting for its progressive stiffness degradation.

Numerical Modeling

The aim of replicating the slippage and cracking phenomena observed experimentally led to the development of numerical models based on nonlinear analysis (for the most, nonlinear static analysis).

To reproduce shear–bond tests, spring models were proposed by Grande and Milani (2018) and Bertolesi et al. (2019): a linear behavior was assigned to the masonry support and the reinforcement, while a nonlinear behavior was considered for the upper mortar layer and for the interfaces of the reinforcement.

The same authors also proposed a two-dimensional (2D) model based on quadrilateral plane stress elements (for the masonry support and the mortar, along the thickness) and truss elements (for the reinforcement). Zero-thickness elements were introduced for the interface between the reinforcement and the mortar layer; nonlinear constitutive laws were assumed for the materials and the interfaces. Grande et al. (2013) also added some local discontinuity between the TRM and the substrate, to represent the presence of weak-bond mortar joints. Razavizadeh et al. (2014) assumed elastic behavior for the materials and introduced nonlinear interfaces both between the reinforcement and the matrix and between the matrix and the masonry. Tamborrino et al. (2021) modeled linear-elastic plane stress and truss elements, for the mortar and the yarns, and introduced line-to-line interfaces with a linear bond slip law, for the yarn–mortar interface, and point-to-point interface with infinitely rigid behavior to couple the upper and lower mortar layer; the masonry substrate was simply replaced by fixed boundaries. The main hypothesis of the 2D model developed by Donnini et al. (2018) were plane strain state, brittle fracture for the matrix and the fibers, and bond–slip nonlinear behavior at matrix–fiber interface.

In three-dimensional (3D) models of shear–bond tests, the plasticity is typically lumped at the interfaces: Carloni et al. (2018) modeled linear-elastic solid elements and introduced three types of zero-thickness interfaces to account for the debonding at the matrix–fiber interface, for the interlaminar failure of the matrix (inner–outer layers), and for the detachment from the substrate. The interfaces accounted for both Mode-II and Mode-I fracture mechanics by means of nonlinear contact laws. Carozzi et al. (2014) considered rigid and indefinite resistant elements (solid for the masonry and the matrix, truss for the reinforcement) connected by means nonlinear elements (quadrilateral interfaces and axial springs, respectively); the reinforcement interacted with the mortar by means of nonlinear interfacial tangential stresses.

The numerical simulation of direct tensile tests on TRM systems was performed by Larrinaga et al. (2014), by adopting a 3D smeared crack model with eight-node solid elements for the mortar and truss elements for yarns; the materials had a nonlinear behavior. The model allowed a feasible reproduction of the crack pattern; the analyzed configurations resulted almost independently from the bond–slip curve governing the interface between the reinforcement and the mortar (thus, perfect bond was assumed in a simplified way). Bertolesi et al. (2014) considered a 2D model through the thickness of the sample, with plane–stress elements for the mortar and truss elements for the yarn. A brittle behavior was adopted for the yarns and perfect bond with the matrix was assumed; different material models were instead considered for the mortar:
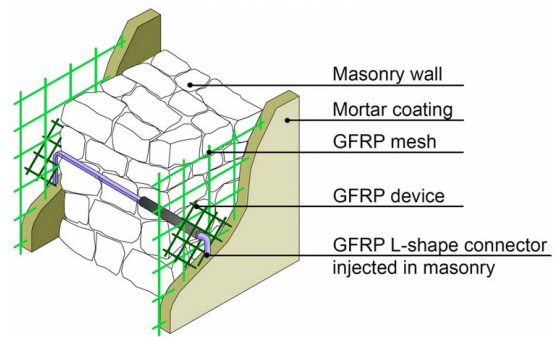

Fig. 2. Schematization of the considered CRM reinforcement technique.

elastic-perfectly-plastic law with limited ductility, or with more sophisticated softening laws. The effects of reinforcement nonplanarity of specimen bending and of preexisting microcracks were investigated. Nerilli et al. (2020) studied the behavior of a single unit cell of TRM by combining three superimposed layers of plane stress and linear-elastic elements, representing the two outer layers of mortar and the inner layer made of fibers and mortar. Three types of interfaces were introduced to account for the mortar cracking (intralayer interface), for the fiber–mortar slippage both within the inner layer (intralayer interface), and between the inner and the outer layers (interlayer interface). The cell units were subjected both to tension and to in-plane shear loading. It was generally concluded that damage is governed by the intralayer interfaces, while interlayer ones do not provide a significant influence; moreover, for a more accurate prediction of the shear behavior at advanced strain levels, also the mortar crushing has to be considered.

Considering the outcomes of the available studies, it is observed that there is not a unique numerical model applied for the simulations of the different types of TRM characterization tests and that, depending on the case, only selected failure modes are considered. Instead, the modeling approach herein presented is proved to be capable for the simulation of the different setups (i.e., tensile, shear bond, and in-plane shear tests), considering the possible damage and collapse mechanisms that can affect both individual materials and their interactions. Moreover, the influence of transversal yarns, orthogonal to the main direction, is taken into account for, and a broad sensitivity study is conducted.

Strengthening Characteristics and Experimental References

In this study, a type of TRM reinforcement called composite reinforced mortar (CRM) is taken into consideration. The technique consists in the application of a fiber-reinforced polymer mesh on the faces of the masonry wall, embedded in a mortar layer having a nominal thickness of 30 mm (Fig. 2). Fiber-based L-shape connectors injected into the masonry and provided with mesh devices are also applied.

The wires of the fiber-reinforced polymer meshes are composed of long AR-glass fibers. The dry fiber wires are soaked in a thermo-hardening resin made of epoxy vinylester, with benzoyl peroxide as catalyst. Then, before the resin harden, the mesh is formed by twisting the wires in one direction (warp) across the wires in the perpendicular direction (weft), which fibers remain parallels. Typically, each wire has an area of dry fibers equal to 3.8 mm^2; the main characteristics of the wires are detailed in Table 1 (Type "S"). Wires of doubled dry fibers area (Type "D" in Table 1) are also available,

Table 1. Main mechanical characteristics of the meshes: dry fibers and gross cross section ($A_{w,\text{fib}}$, $A_{w,\text{tot}}$), gross perimeter (t), tensile strength (T_w), Young's modulus (E_w), and mesh intersections resistance (K). The coefficients of variation are also reported

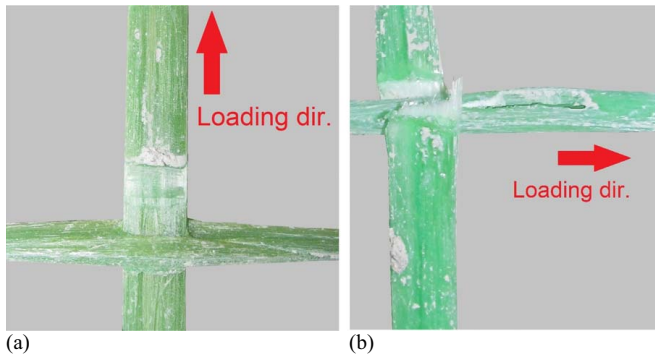| Glass-fiber wires	$A_{w,fib}$ (mm^2)	$A_{w,\text{tot}}$ (mm^2)	t_w (mm)	T_w (kN)	c.o.v. (%)	E_w (GPa)	c.o.v. (%)	K (kN)	c.o.v. (%)
Parallel fibers wire, Type S	3.8	9.41	18.0	5.62	4.8	69.5	5.7	0.55	19.9
Twisted fibers wire, Type S	3.8	7.29	9.57	4.49	6.7	62.9	9.5	0.48	23.6
Parallel fibers wire, Type D	7.6	21.4	24.5	10.4	5.5	71.6	10.8	1.13	20.3
Twisted fibers wire, Type D	7.6	14.1	13.5	7.06	3.6	67.5	22.3	0.93	28.0

Fig. 3. Typical failure mode of the mesh intersections in the direction of (a) parallel or (b) twisted fiber wires.

even though they are less frequently used. Usually, the mesh has a squared grid pitch of 66×66 mm^2; meshes having grid pitches 33×33 mm^2 and 99×99 mm^2 are also available.

The resistance of the mesh intersections, tested accordingly to CEN (2019a), is also reported in Table 1: coherently with the mesh production process, the joint resistance along the parallel fibers wire direction is mainly due to the presence of the thermosetting resin [Fig. 3(a)], differently, along the twisted fibers wire direction, the orthogonal fibers oppose to the slip and progressively shear out [Fig. 3(b)].

Extensive experimental results are available in the literature for this technique, in terms of materials and CRM system characterization (Gattesco and Boem 2017a; Sisti et al. 2019), as well as of CRM-strengthened masonry walls performances for in-plane and out-of-plane loading (Gattesco and Boem 2015, 2017b). The main experimental evidence concerning the CRM mechanical characterization (pullout, tensile, shear bond, and in-plane shear tests) are summarized in this section, to allow comparison with the numerical outcomes. More-detailed reports concerning the pullout, tensile, and shear bond tests are available in Gattesco and Boem (2017a); the experimental results of the in-plane shear tests can instead be found in Sisti et al. (2019).

In the considered tests, the matrix was made by mixing 300 kg of hydraulic lime and 100 kg of Portland cement per m^3 of mortar, calcareous sand (with grain diameter range 0.5–2.0 mm), and water addition until attainment of a smooth consistency. The average mechanical characteristics of the mortar were assessed through tests on mortar cylinders (100 mm in diameter and 200 mm in height) after 28 days of air curing. The tests provided an average compressive strength $f_c = 6.3$ MPa (c.o.v. 11%), a tensile strength $f_t = 1.1$ MPa (c.o.v. 8%), and a Young's modulus of $E = 14.43$ GPa (c.o.v. 14%) (CEN 2009, 2019b, 2021).

Pullout Tests

Pullout experimental tests concerned $180 \times 180 \times 30$ mm^3 CRM coupons, in which the central wire of the 66×66S mm^2 mesh was gradually pulled out (effective bond length: 120 mm); the

displacement between the central wire and the mortar-coated pulled edge was measured (base length: 140 mm). Tests were performed with the twisted fiber wires along both the loading direction (PO-T-66S) and orthogonal (PO-P-66S).

The former arrangement evidenced a progressive failure due to the wire extraction [Fig. 4(a)] or, sometimes, to the rupture of the central wire (mean load 4.14 kN, c.o.v. 10.3%). In the latter [Fig. 4(b)], the wire extraction always occurred (mean resistance 4.08 kN, c.o.v. 14.3%). The experimental force–displacement curves [Fig. 4(c)] evidenced a progressive wire detachment from the mortar, from about 30%–35% of the peak load. After the peak load, a brittle behavior resulted in samples with the wire failure, while a gradual resistance decrease was observed in the other cases (more pronounced when pulling the parallel fibers wire).

Tensile Tests

The experimental direct tensile tests on CRM were performed on coupons of two different dimensions: $900 \times 132 \times 30$ mm^3 and $1{,}220 \times 132 \times 30$ mm^3, identified as Types "a" and "b," respectively. In both cases, the clamping heads were created by wrapping the extremities with FRP carbon strips, for a length of 132 mm. In Type "b" samples, the mortar discontinuity was created at the clamps. The samples were provided with a 66×66S mm^2 mesh, having the twisted fiber wires disposed in the loading direction. A monotonic loading was applied, at displacement control.

During the tests, transversal cracks generally formed in the mortar, in the vicinity of the transversal wires and the average distance between cracks ranged from 1 to 2 grid pitches, as can be observed, for example, in Fig. 5(a) (TS-Ta-66S, Type "a" samples) and Fig. 5(b) (TS-Tb-66S, Type "b" samples). The obtained equivalent stress–strain curves are also reported in Figs. 5(a and b) (the stresses refer to the dry fibers cross section); no significant differences emerged from the two sample types. The tests provided a trilinear behavior, with the uncracked stage until about $\varepsilon = 0.01\%$ and the cracked stage starting from about $\varepsilon = 0.55\%$. The first cracking occurred at about 4.9 kN (c.o.v. 10.4%) and the failure at 11.32 MPa (c.o.v. 11.8%), due to the wires' breakage. A tension–stiffening effect of the intact mortar between the cracks was observed.

In addition, Type "a" samples provided with a 99×99S mm^2 mesh and having the twisted fiber wires disposed in the loading direction were tested (TS-Ta-99S); in this case, the width of the samples was 198 mm. The third stage of the equivalent stress–strain curves was interrupted by the premature failure for the mesh slippage at the ends [Fig. 5(c)]. The ultimate tensile strains are more scattered, depending on the position of the outer cracks in respect the measurement base length.

Shear–Bond Tests

Shear–bond tests concerned solid brick masonry wallets ($250 \times 315 \times 120$ mm^3) to which the CRM layer (30 mm thick, 132 mm wide, and a mesh of 66×66S mm^2) was applied on one face, with the twisted fiber wires oriented in the loading direction. Three different bond lengths were considered: $l_b = 120$–180–240 mm. The samples were subjected
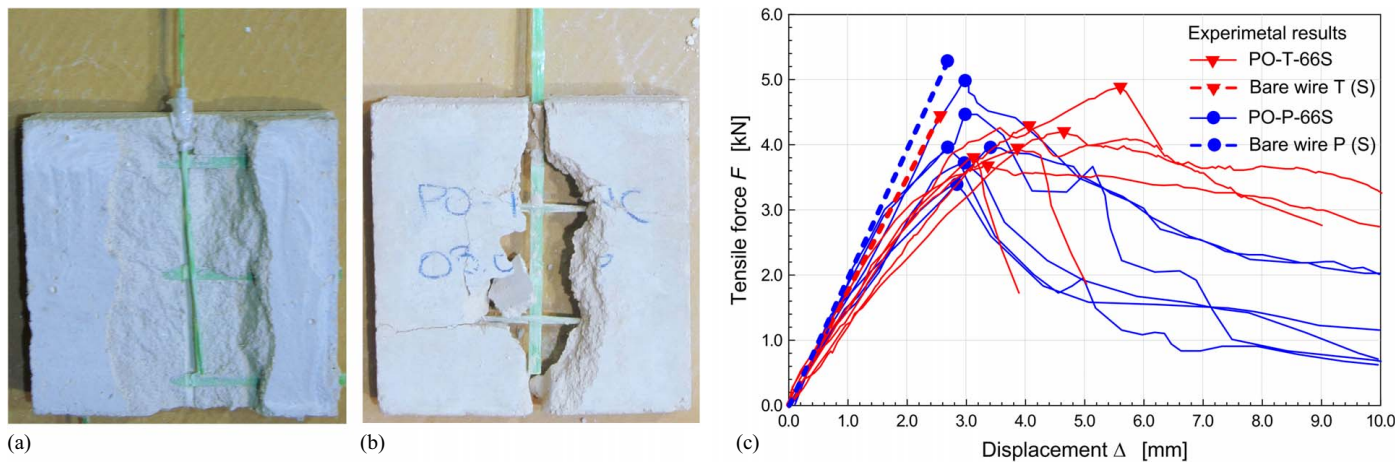
Fig. 4. Experimental pullout tests: typical failure mode for (a) PO-T-66S and (b) PO-P-66S samples. The force–displacement curves are plotted in (c).
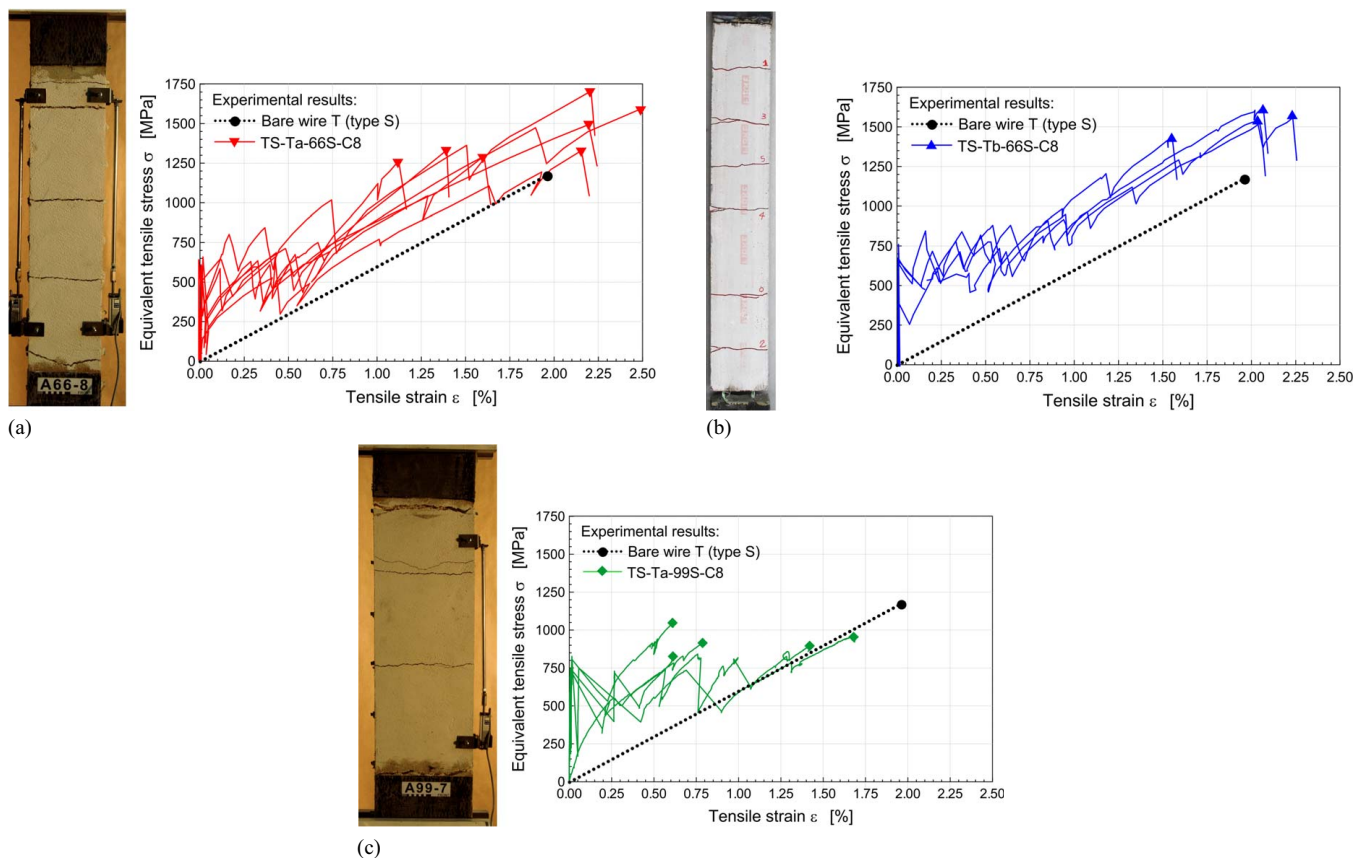

Fig. 5. Experimental tensile tests: typical crack pattern and stress–strain curves of (a) TS-Ta-66S; (b) TS-Tb-66S; and (c) TS-Ta-99S.

to monotonic loading at displacement control. The relative displacement between the exceeding mesh and the mortar-coating edge was surveyed (base length 100 mm), as well as that between the mortar coating and the masonry support. The curves are plotted in Fig. 6(a).

The tests provided different results, depending on the bond length: for $l_b = 120$ mm (SB-T120-66S), the failure was due to slip at the mesh–matrix interface [mean peak load 6.5 kN, Co.V. 18%, Fig. 6(b)]; for $l_b = 240$ mm (SB-T240-66S) the longitudinal wires rupture was reached (at 9.5 kN, c.o.v. 5%); the bond length $l_b = 180$ mm (SB-T180-66S) resulted as the minimum bond length for the CRM reinforcement, as collapse due both to the wires rupture and to the mesh–matrix slip were observed (mean peak load

9.3 kN, Co.V. 2%). Typically, the former resulted in a more brittle behavior, in respect the second one. The mortar–masonry slip until failure always resulted negligible (<0.05 mm). Also, the $33 \times 33S$ mm^2 mesh was tested for $l_b = 240$ mm, (SB-T240-33S): in this case, the failure for the wires collapse or for the deboning of the mesh-to-mortar interface [Fig. 6(c)] occurred for very similar force values (16.4 kN, c.o.v. 6%).

In-Plane Shear Tests

In-plane shear tests concerned CRM panels with dimensions $1,000 \times 1,000 \times 30$ mm^3 [IS-P-66S, Fig. 7(a)] provided by a
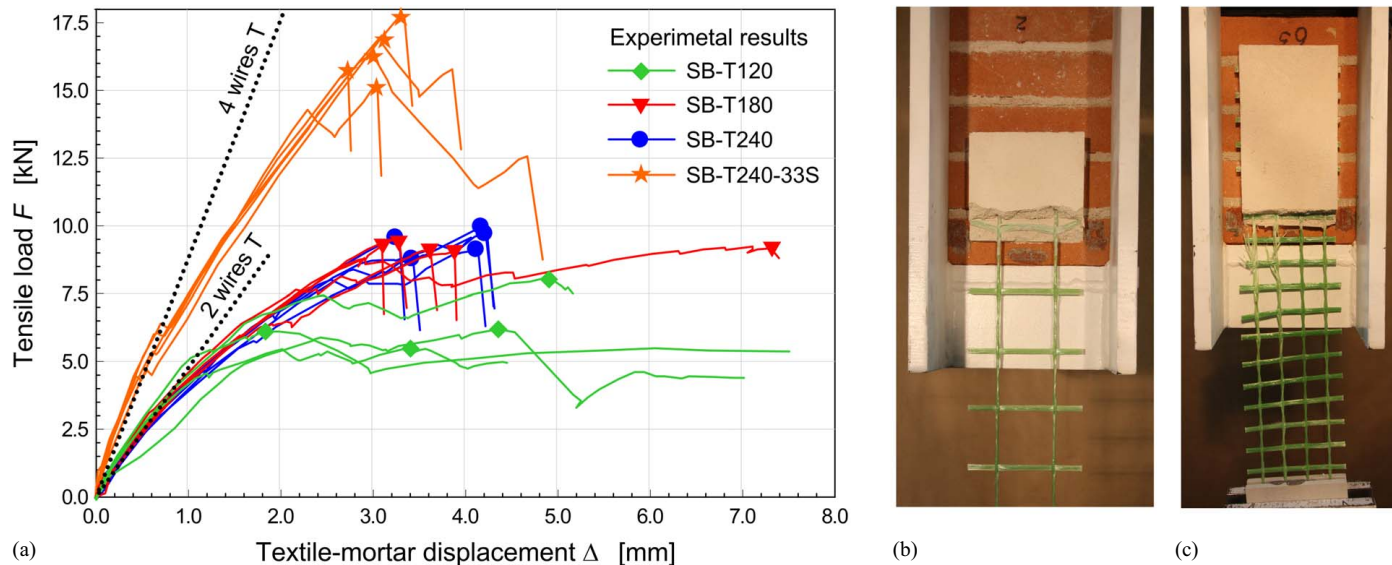
Fig. 6. Experimental shear–bond tests: (a) load against textile-mortar displacement curves; (b) failure for mesh-matrix slip in SB-T120-66S; and (c) failure for slip and debonding in SB-T240-33S.
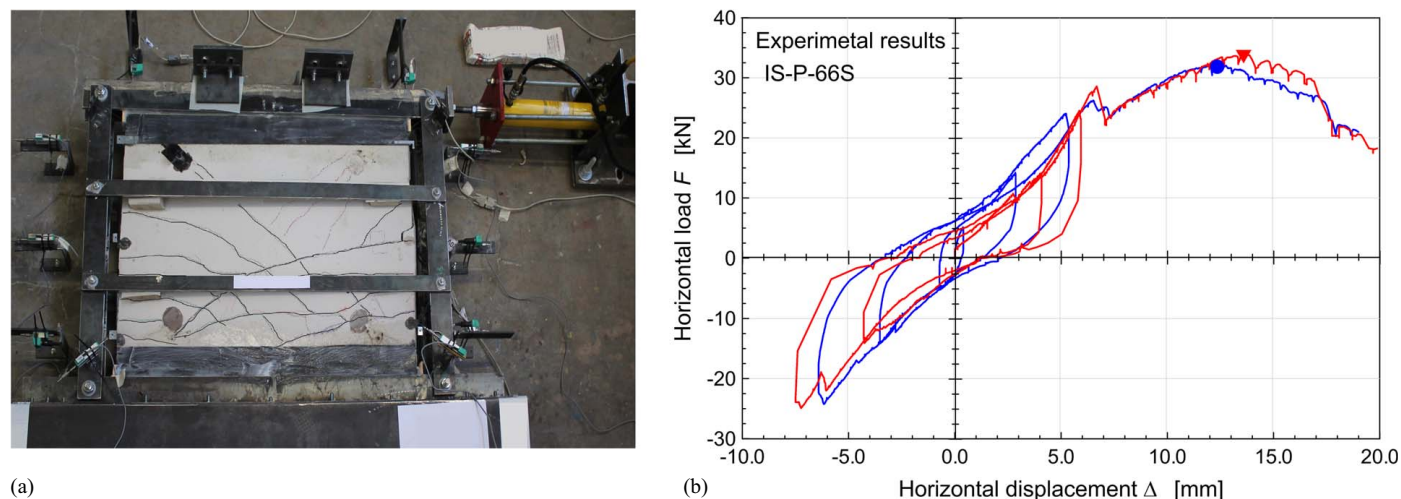

Fig. 7. Experimental in-plane shear tests: (a) typical crack pattern; and (b) horizontal load–displacement curves.

mesh of $66 \times 66S$ mm^2, with the parallel fiber wires disposed vertically. The upper and lower edge were strengthened with FRP carbon strips (about 180 mm in height) glued to a squared steel frame, with pinned nodes fixed at the base and loaded horizontally at the top (cyclic loading, displacement control).

At the increasing of the displacement, several cracks formed progressively, starting from the bottom to the top of the sample, inducing a gradual stiffness reduction. The cracks started with a horizontal trend, near the tensed side, almost in correspondence of the wires, and then followed an inclined trend as long as they prosecuted toward the center of the panel. Some diagonal cracks also appeared, almost at the end of the test.

The curves representing the applied load at the varying of the horizontal displacement at the top are plotted in Fig. 7(b). The peak load was reached at about 33.0 kN at 13.1 mm; then, a decrease of resistance occurred, accompanied with the slippage or breakage of some wires and damaging of mortar. By analyzing the envelope curves, an increase in stiffness emerges in the branch

2–5 mm, compared with the previous one, as already noticed by Sisti et al. (2019), but this occurrence is realistically related to the shear behavior of the tightened bolts at the base connection (Lin et al. 2021).

Calibration of the Numerical Model

The numerical model was developed by using a free, open-source, finite-element code (Patzák and Bittnar 2001; Patzák 2012). Details concerning the mentioned elements and materials models are available in the manuals section of the code webpage (Patzák 2002). The input files of the models herein described are available for free consultation and use (Boem 2021b).

The detailed level numerical model [Fig. 8(a)] was composed of linear 3D brick finite elements (*LSpace*), dimensions $16.5 \times 16.5 \times 15$ mm^3, representing the mortar, and linear isoparametric truss elements (*truss3d*), length 16.5 mm, for the embedded reinforcement.
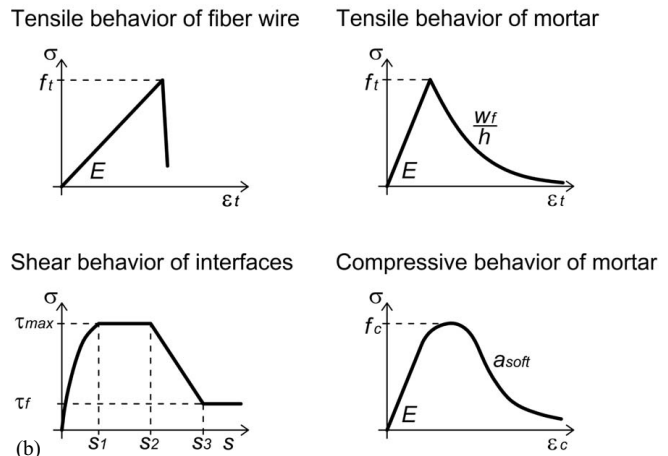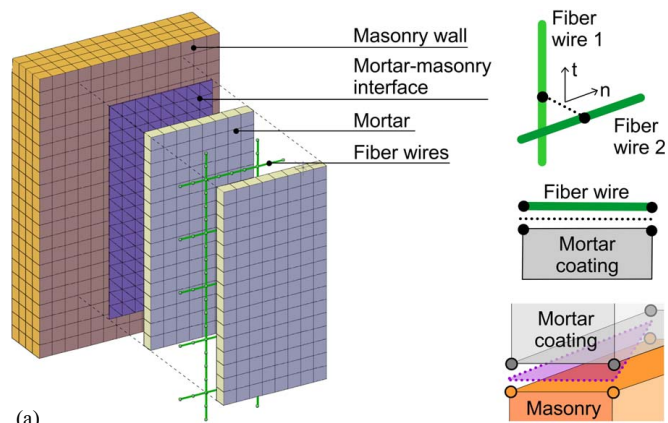
04022060-7

Fig. 8. Schematization of the detailed level model: (a) global view and details of the mesh intersections, the wire–mortar interaction and the mortar–masonry interface; and (b) main constitutive laws considered.

Orthogonal wires were connected at the mesh intersections by means of point-to-point interface elements (*IntElPoint*). *IntElPoint* is a one-dimensional (1D) (slip) interface element that can be used to connect two separate nodes, and the interaction is governed by a 1D slip law. This law determines the force acting between the nodes as a function on their relative displacement in the slip direction. The truss elements, representing the wires, were connected to the edge of the solid elements, representing the mortar, by using line-to-line interface elements (*IntElLine1*) oriented in the wires' direction. *IntElLine1* is a 2D line element with a linear approximation of the displacement jump; the element can be used to tie together two element edges and is defined by four nodes (two on each edge). The masonry wallets in the shear–bond tests were modeled by means of 3D brick finite elements (*LSpace*), with dimensions of $16.5 \times 16.5 \times 15$ mm^3; since negligible deformations were monitored during the experimental tests, an equivalent homogeneous, isotropic material, with indefinitely elastic behavior was assumed, for sake of simplicity. To connect the mortar coating to the masonry substrate, 3D surface interface elements with linear approximation were adopted (*IntElSurfTr1*). The analyses were performed under displacement control, by using the Newton–Raphson solver and a relative convergence norm set to 10^{-3} displacement and force.

The calibration of the materials parameters [Figs. 8(b) and 9] was generally achieved through comparison with the available experimental results obtained from tests on single elements (wires, mesh interfaces, mortar cylinders).

In particular, for the wires, an isotropic damage model (*idm1*) was assumed, accounting for the well known brittle rupture behavior in tension; the main characteristics were taken from to the experimental outcomes of direct tensile tests (Table 1).

For the mortar of the coating, a concrete-damage plasticity model (Grassl and Jirásek 2006) was calibrated (*con2dpm*), to account for both cracking and crushing; the Young's modulus and the compressive and tensile strengths were set in accordance to

GFRP WIRE			Wires, type S		Wires, type D	
			Twisted	Parallel	Twisted	Parallel
Element type			Truss3d	Truss3d	Truss3d	Truss3d
Material type			idm1	idm1	idm1	idm1
Cross section	A	[mm^2]	3.8	3.8	7.6	7.6
Young modulus	E	[GPa]	62.9	69.5	67.5	71.6
Poisson modulus	n	[-]	0.3	0.3	0.3	0.3
Softening law	-	[-]	Linear	linear	Linear	linear
Peak strain	ε_0	[%]	1.88	2.12	1.38	1.92
Ultimate strain	ε_t	[%]	1.90	2.20	1.60	2.10
MESH INTERSECTIONS						
Element type			intElPoint	intElPoint	intElPoint	intElPoint
Material type			bondceb	bondceb	bondceb	bondceb
Normal stiffness	K_n	[N/mm]	0	0	0	0
Tang. stiffness	K_t	[N/mm]	10000	10000	10000	10000
Bond parameters	T_{max}	[N]	458	550	930	1131
	T_f	[N]	0.0	0.0	0.0	0.0
Slip parameters	s_1	[mm]	0.5	0.5	0.5	0.5
	s_2	[mm]	1.5	0.5	1.5	0.5
	s_3	[mm]	10.0	0.6	10.0	0.6
WIRE-MORTAR CONNECTION						
Element type			intElLine1	intElLine1	intElLine1	intElLine1
Material type			bondceb	bondceb	bondceb	bondceb
Equiv. perimeter	t	[mm]	9.57	18.0	13.5	24.5
Normal stiffness	k_n	[N/mm^2]	1000	1000	1000	1000
Tang. stiffness	k_t	[N/mm^2]	1000	1000	1000	1000
Bond parameters	τ_{max}	[MPa]	3.3	2.0	3.3	2.0
	τ_f	[MPa]	2.2	0.25	2.2	0.25
Slip parameters	s_1	[mm]	0.1	0.1	0.1	0.1
	s_2	[mm]	0.1	0.1	0.1	0.1
	s_3	[mm]	1.2	1.2	1.2	1.2

MORTAR COATING			
Elem. type			LSpace
Mat. type			con2dpm
Young modulus	E	[GPa]	14.4
Poisson modulus	n	[-]	0.25
Comp. strength	f_c	[MPa]	6.29
Tens.strength	f_t	[MPa]	1.10
Dilation coeff.	arctgψ	[-]	0.85
Softening law	-	[-]	Linear
Hardening param.	b_h	[-]	0.002
	h_p	[-]	0.0
Softening param	w_f/h	[-]	0.011
	a_{soft}	[-]	4.0
MASONRY			
Elem. type			LSpace
Mat. type			con2dpm
Young modulus	E	[GPa]	4.3
Poisson modulus	n	[-]	0.45
MORTAR-MASONRY CONNECTION			
Elem. type			intElSurfTr1
Mat. type			bondceb
Normal stiffness	k_n	[N/mm^3]	10000
Tang. stiffness	k_t	[N/mm^3]	500
	τ_{max}	[MPa]	1.175
	τ_f	[MPa]	0.05
	al	[-]	0.55
Slip parameters	s_1	[mm]	0.04
	s_2	[mm]	0.05
	s_3	[mm]	0.10

Fig. 9. Main characteristics of elements, materials, and interfaces in the numerical model. For unspecified parameters, the code default values were set. (Data from Patzák 2002.)
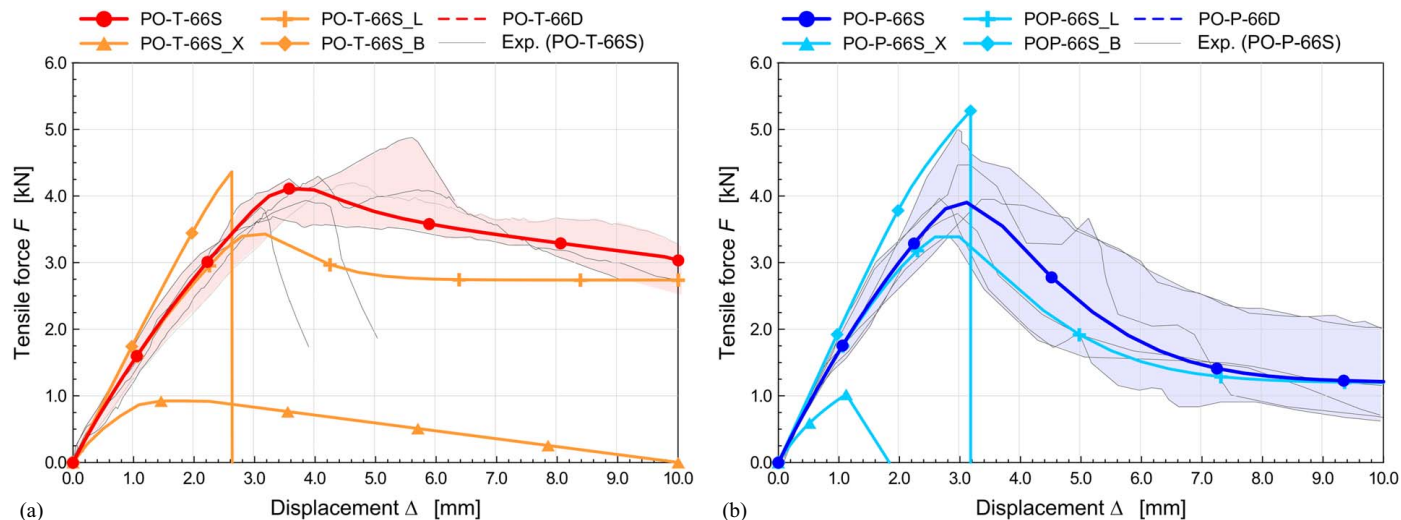
Fig. 10. Pullout tests: numerical curves, in comparison with the experimental results, for load applied in the direction of the (a) twisted or; and (b) parallel fiber wires.

the experimental characterization tests performed on mortar cylinders (compression tests and indirect tensile tests).

For the point-to-point interfaces, representing the intersection between orthogonal wires, the bond–slip nonlinear model reported in the CEB Model Code for Concrete Structures (CEB 2010) was considered in the tangential direction (*bondceb*); the governing parameters were set in accordance with the experimental outcomes on mesh intersections (Table 1): a stronger but brittle behavior in the direction of the parallel fiber wires, instead of a quite weaker (−13%) but more ductile behavior in that of the twisted wires.

Also, for the line-to-line interfaces, the bond–slip model for reinforced concrete (*bondceb*) was applied, with the tangential component described by a nonlinear function. The calibration procedure is described in the next subsection.

Pullout Tests

For the calibration of the bond–slip relationships governing the wire–mortar interactions, the experimental pullout tests described in the previous section were simulated by keeping constant all the other material parameters, already determined, and calibrating the characteristics of the linear interface elements, to reproduce as accurately as possible the mean results of these tests.

The shear–bond strength of the twisted fiber wires ($\tau_{max} = 3.3$ MPa) resulted in reasonably higher value than that of the parallel fiber wires ($\tau_{max} = 2.0$ MPa), due to the greater roughness; however, due to the lower contact perimeter (t), the tangential resistance per unit of length ($v = \tau_{max} \cdot t$) was comparable; the residual resistance (τ_f) was higher for the twisted fibers wire, accordingly to a better residual friction. The calibrated bond–slip curves resulted in agreement with those reported in the literature for similar fiber-based elements embedded in an inorganic matrix (Cosenza et al. 1997; Focacci et al. 2017). The numerical results are reported in Fig. 10 (id. PO, followed by -T or -P, for the twisted or parallel fibers wires oriented along the loading direction, respectively, and the mesh type -66S). The different interface contributions were also investigated: presence of point interface only (suffix _X), of line interfaces only (_L), and perfect bond between the wires and the mortar (_B). The global performances in the two loading directions are comparable until the attainment of the peak load, at about 4 kN, but then the

resistance decrease is more gradual for the loading along the parallel fibers wire direction (at $\Delta = 10$ mm, the load is about 3 kN, instead of 1.2 kN). This is due to both the better residual friction of the twisted wires (compare the _L curves) and to the higher displacement capacities of the mesh intersections in this direction (compare the _X curves). The pullout behavior is mainly governed by the wires–mortar interfaces; however, the mesh intersections provide an improvement of the performances. Under the assumption of perfect bond (_B), the wire rupture occurs, accompanied by some mortar splitting; it is however observed that, in actual applications, the masonry substrate counteracts this latter occurrence.

The tangential forces per unit of length v measured along the central wire at the varying of the distance l_i from the pulled edge are plotted in Fig. 11. Different levels of displacement Δ are considered, ranging from 0.5 to 5 mm. At the beginning, the tangential forces are mainly concentrated in the initial wire portion but then spread progressively, involving the entire bond length when approaching to the peak load. Then, the residual values of resistance are attained. As expected, when the contribution of the mesh intersections is neglected (_L), higher values of unitary force v result for the same displacement level Δ; thus, the debonding is anticipated.

To evaluate the model sensitivity to the meshing discretization, the pullout tests were also simulated considering a finer element discretization ($8.25 \times 8.25 \times 7.5$ mm^3), and analogous results were obtained. Differently, a coarser discretization ($33 \times 33 \times 15$ mm^3) was too rough to accurately investigate the trend of the shear stresses along the wires for detailed modeling purposes.

Since no masonry damaging was observed in the shear bond experimental tests, an elastic material model was assumed for the masonry (*isoLE*), with elastic properties in agreement with previous experimental outcomes (Gattesco and Boem 2017b). The *bondceb* material model was considered for the tangential stress–strain relationship governing the interaction between the CRM layer and the masonry support. The main parameters were set in accordance with some experimental tests and numerical studies available in the literature on masonry bed joints coupling bricks and mortar with characteristics similar to those herein (Van der Pluijm et al. 2000; Zhang et al. 2018; Barattucci et al. 2020).
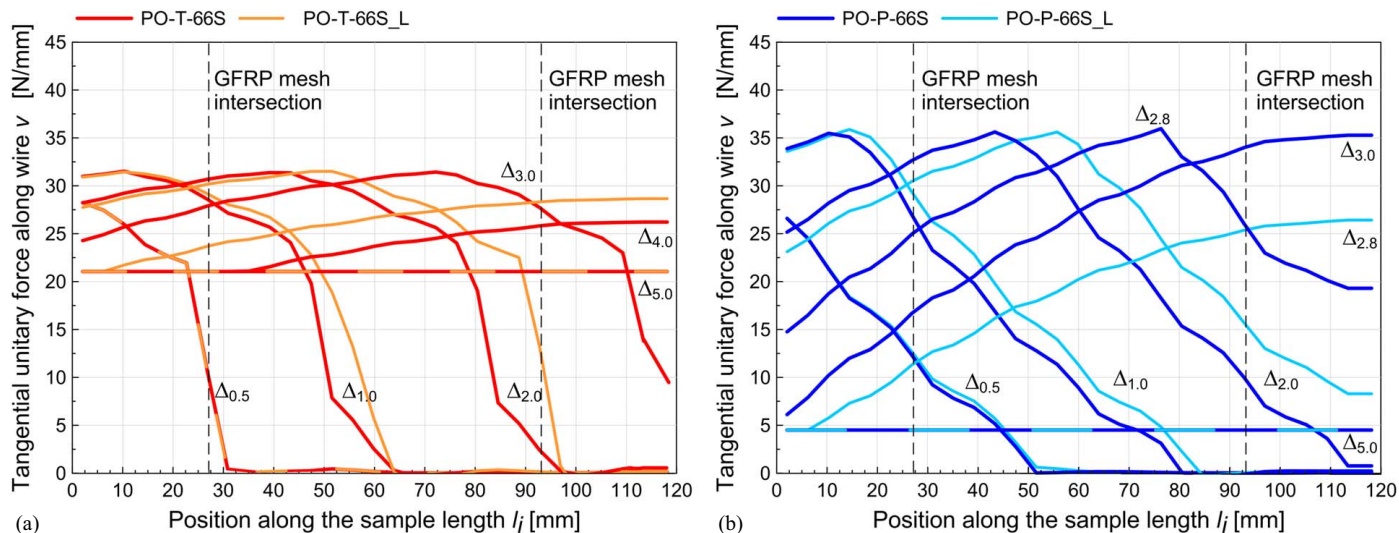
Fig. 11. Pullout tests: trend of the central wire tangential unitary force at different displacement levels (in mm), for load applied in the direction of the (a) twisted or; and (b) parallel fiber wires.
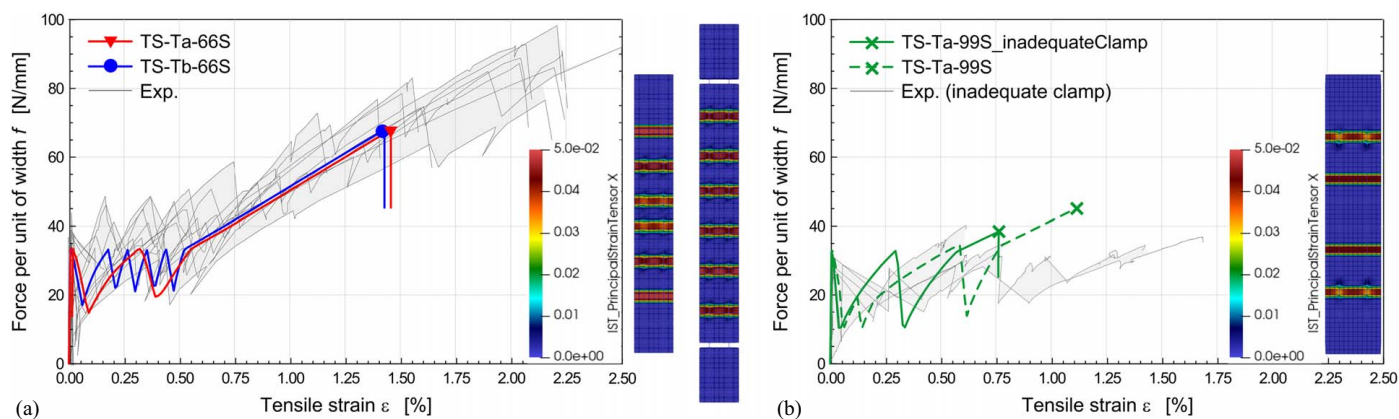

Fig. 12. Direct tensile tests: numerical curves of (a) -66S; and (b) -99S samples, in comparison with the experimental results and illustration of the principal tensile strains in the mortar at peak load, to highlight the cracks position.

Validation of the Numerical Model

To validate the numerical model, the direct tensile tests, the shear–bond tests, and the in-plane shear tests on CRM samples previously described were considered for comparison.

Tensile Tests

The numerical results of the direct tensile tests are plotted in Fig. 12, in terms of force per unit of width of the CRM layer, at the varying of the equivalent tensile strain. The ID for this numerical model is TS; suffix -T indicates the twisted fiber wires oriented along the loading, and label "a" or "b" refers to the different sample type; moreover, the grid size and type are distinguished (-66S and -99S).

The numerical results obtained from the two different test types on -66S samples [Fig. 12(a)] are comparable, as well as those from the experimental tests, to which the general trend is in agreement: there is a first elastic branch, for $\varepsilon < 0.01\%$, with high stiffness; then, as the first crack occurred (at 4.4 kN), there is a jagged second stage, with sequential formation of transversal cracks, and a final linear stage, within the range $\varepsilon = 0.50\%$–1.45%, ending with the

attainment of the longitudinal wires failure at 9.0 kN. More cracks formed in the Type "b" sample, with respect to the Type "a" sample, due to the higher length.

Actually, the experimental local force peaks at the formation of each crack were more scattered, as affected by some intrinsic variability in the mortar tensile strength (c.o.v 8%) and by possible irregularities in the effective mortar cross section, as will be later confirmed by the sensitivity analysis. Moreover, higher resistance values were often reached in the experimental tests, in respect to the numerical provisions: this was due, more than to the variability of the actual wires resistance (c.o.v. 6.7%), to the presence of the mortar matrix, which provided an additional constrain to the untwisting of the wires, improving their resistance; differently, in the numerical simulations, the values obtained from the characterization tests on single bare wires were considered (Table 1).

The evolution of the principal tensile strains in the mortar layer are reported in Fig. 13(a): it can be observed that the main cracks in the mortar are located in correspondence of the transversal wires, at a distance of 132 mm, according to the experimental pattern [Fig. 5(b)]. The tensile stresses along the wires, plotted in Fig. 13(b), evidence peak values in
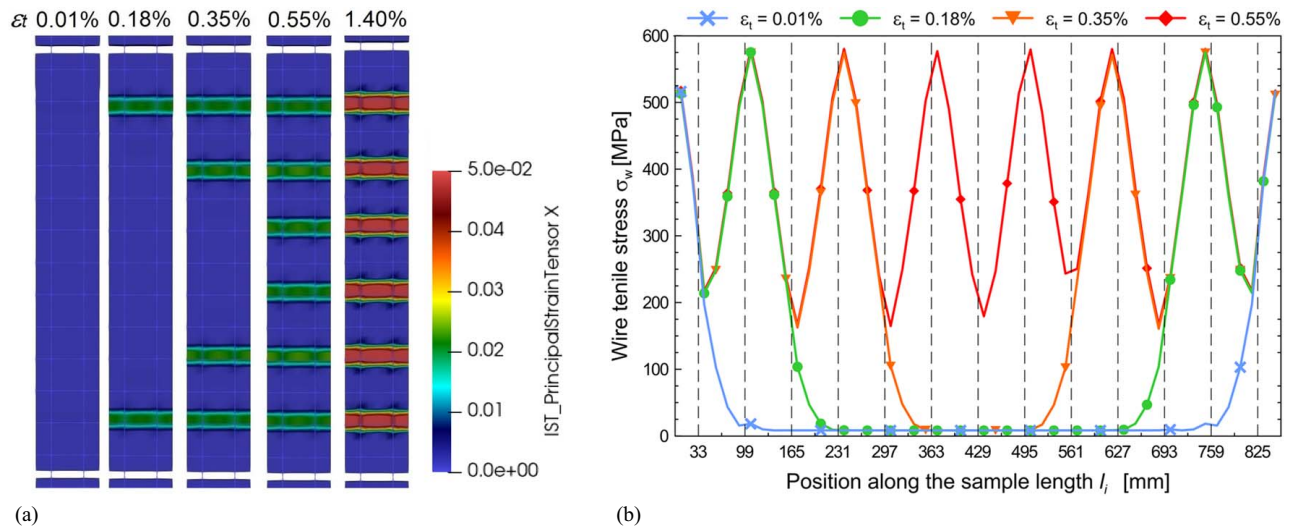
Fig. 13. Sample TS-Tb-66S: evolution of (a) mortar principal tensile strains; and (b) wires tensile stresses.
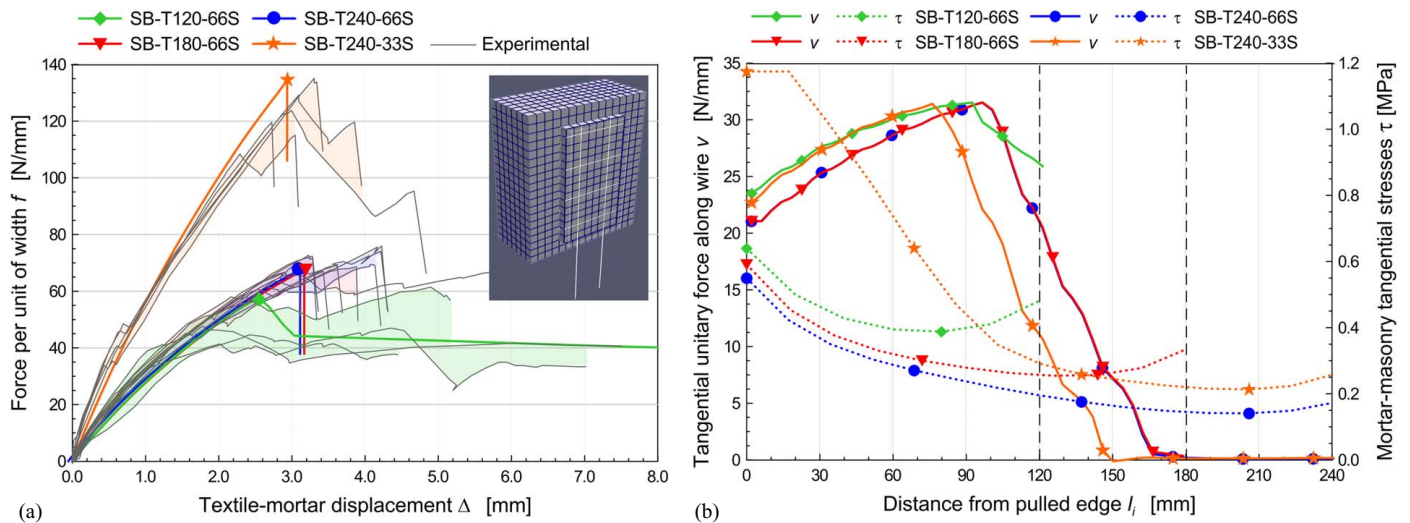

Fig. 14. Shear bond tests: (a) numerical curves, in comparison with the experimental results; and (b) distribution of the tangential forces in the wire–mortar, v, and mortar–masonry, τ, interfaces, at peak load.

correspondence of the cracks in the mortar. The simulation of test TS-Ta-99S [Fig. 12(b)] confirmed the occurrence of the premature failure for the yarn's slippage at the grips. In fact, in this case, only one transversal wire was effectively located inside the clamps, instead of the three yarns in the TS-Ta-66S samples. Considering an adequate clamp, the wires failure can be reached, and quite higher load and ultimate strain are attained; however, the resistance is reasonably lower in respect to TS-Ta-66S (according to the grid pitch).

Shear–Bond Tests

The numerical results of the shear–bond tests and the comparison with the experimental ones are reported in Fig. 14(a), in terms of force per unit of width, f, under the increasing displacement Δ between the unbonded mesh and the mortar coating. The ID for this numerical model is SB-T (suffix -T refers to the twisted fiber wires oriented along the loading direction); followed the indication of the bond length (120, 180, or 240) and of the grid size and type (e.g., -66S, -33S).

Considering the scatter in the experimental parameters of materials and interfaces, the numerical results are in good agreement with the mean experimental outcomes, both in terms of f-Δ capacity curves trend and failure modes. Indeed, when a bond length l_b of 120 mm was investigated (SB-T120-66S), the failure for the slippage of the longitudinal wires from the mortar occurred, at 7.6 kN ($\Delta = 2.6$ mm); then the load tuned down to about 5.8 kN and then very gradually decreased. Also, for $l_b = 180$ and 240 mm (SB-T180-66S and SB-T240-66S) some slips were detected (the slope of the f-Δ curves gradually reduced), but the failure was due to the wires rupture out of the bonded area, at 9 kN ($\Delta = 3.2$ mm). Similarly, in SB-T240-33S, for which the ultimate strain of the wires was reached at 18 kN ($\Delta = 2.9$ mm).

The trends of the tangential force per unit of length along the longitudinal wires, v, are plotted in Fig. 14(b), with reference to the peak load f: in -66S samples, perfect bond was detected from a distance $l_i = 165$ mm from the pulled edge, with a peak value of v reached at $l_i = 95$ mm. In SB-T240-33S, perfect bond was detected from a lower distance, $l_i = 150$ mm, with maximum value of v at $l_i = 80$ mm. The tangential stresses at the mortar–
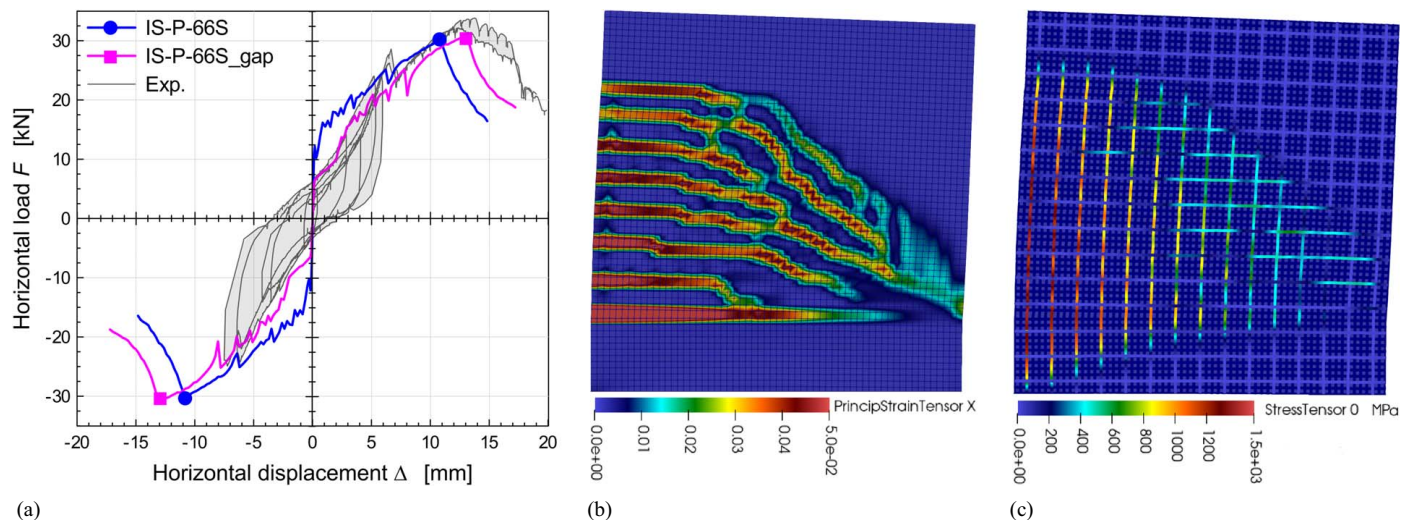
Fig. 15. In-plane shear tests: (a) numerical curves, in comparison with the experimental results; (b) principal tensile strains in the mortar; and (c) tensile stresses in the mesh at peak load.

masonry interface, τ, are also plotted in Fig. 14(b). The typical behavior of shear joints connecting elastic materials was recognized, with higher values at the extremities and an unsymmetrical trend due to the different stiffness of the coupled materials. In the SB-T240-33S sample, the stresses attained to the maximum bond resistance at the pulled edge (τ_{max} in Fig. 9), evidencing that the collapse for debonding from the support was very close to occur.

In-Plane Shear Tests

The numerical capacity curve concerning the in-plane shear tests (labelled IS-P-66S) is reported in Fig. 15(a) in terms of horizontal force F under the increasing horizontal displacement at the top Δ. The numerical model showed an initial high-stiffness branch until about 12 kN, then the first crack formed close to the base, on the left side. At the increasing horizontal displacement, a gradual stiffness decrease occurred since other cracks formed, as evidenced in the damage pattern of Fig. 15(b). The peak load, equal to 30 kN, was attained at $\Delta = 10.8$ mm. The higher tensile stresses in the mesh [Fig. 15(c)] mainly involved the vertical wires on the left, tensed side, which result was also affected by some debonding from the matrix at the base, at the end of the test. Moderate stresses also arose in both the horizontal and vertical wires along the sample diagonal, while the area of the top-right corner was almost undisturbed.

Although the final crack pattern was consistent with the experimental evidence [Fig. 7(a)], the initial high-stiffness branch in the experimental curves ended earlier (5–8 kN), and the subsequent stiffness was lower in respect to the numerical estimations; the curves gained stiffness from about 2 to 5 mm and the gap with the numerical one gradually reduced.

The discrepancy, in this case, rather than to the intrinsic scatter in materials and interfaces properties and dimensions, already mentioned, has to be attributed, more realistically, to the occurrence of some slip in the bolted connection at the base of the experimental samples. As a proof, the simulation "IS-P-66S_gap" [Fig. 15(a)] was performed by introducing, at the sample base, two springs at the opposite corners, accounting for the shear behavior of bolted connections. The springs had a nonlinear behavior characterized by an initial high stiffness (till 6.5 kN, representing the friction

transmission stage related to the bolts tightening), a slip stage with low stiffness (caused by the gap between the holes and the screws, set equal to 0.9 mm), and a bolt-loading stage with high stiffness. In such a way, the trend of the numerical capacity curve appeared more similar to the experimental one.

It should also be observed that, at advanced displacement levels, the nonlinear-static analysis neglected possible cumulative damage due to cyclic loading (e.g., some sliding at the base horizontal crack, which involved the entire sample width, or some degrading of the wires bonding).

Sensitivity Analysis

Parametric analyses were conducted to investigate on the sensitivity of the CRM performances to the main characteristics of the individual components. The different available grid configurations were at first investigated for tensile and shear bond tests [solid lines in Figs. 16(a) and 17]. For the tensile tests simulations, the Type "b" sample and an adequate clamping system were assumed; for the shear bond tests, a 240-mm bond length was considered.

By comparing the performances of the -66S, -33S, and -99S meshes, it emerged that the increase of the reinforcement ratio generally led to higher resistances and stiffer performances. In the tensile tests (Fig. 16), the cracking formation stage was shorter and smoother, as a result of more numerous, thinner, and closer cracks [as observed by comparing the crack pattern at peak loads, in Fig. 16(b)], and the tension stiffening effect decreased. In the shear bond tests (Fig. 17), the trends of the tangential forces along the longitudinal wires at peak load for -99S were almost comparable with -66S ($v \sim 0$ for $l_i = 170$ mm), while for -33S, the slips involved a shorter bond length (about 150 mm), due to the contribution provided by the numerous mesh intersections [Fig. 17(b)].

The presence of Type "D" yarns was also investigated (meshes -66D and -99D); note that the presence of Type "D" yarns determines a variation in the characteristics of the wires, as well as in those of the yarn–mortar interfaces and of the mesh intersections, according to the values reported in Table 1 and Fig. 9. The global behavior of configurations -33S and
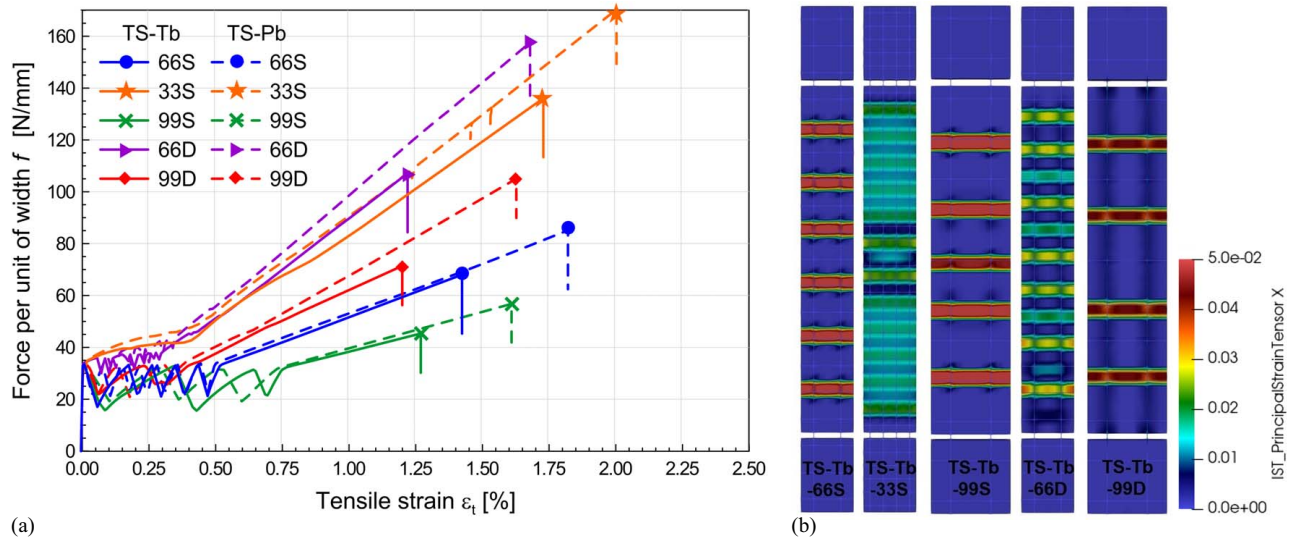
Fig. 16. Sensitivity analysis in tensile tests, with variation of the reinforcement ratio and orientation: (a) capacity curves; and (b) principal tensile strains at peak load.
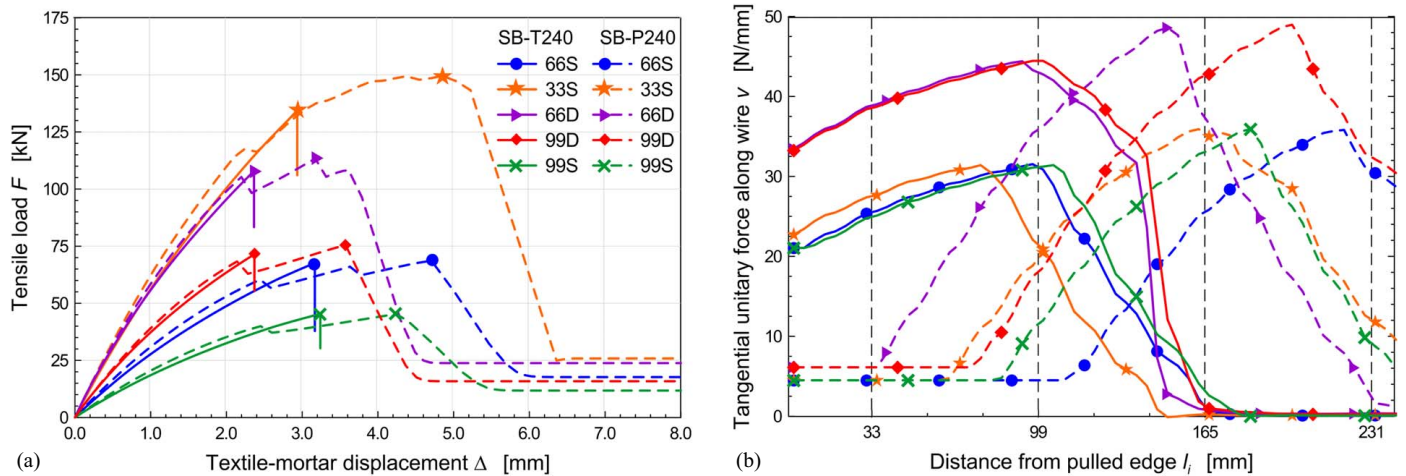

Fig. 17. Sensitivity analysis in shear bond tests, with variation of the reinforcement ratio and orientation: (a) capacity curves; and (b) tangential forces at the wires' interfaces at peak load.

-66D (same reinforcement ratio) was quite similar, but with fewer and thicker cracks in the latter and lower resistances, according to the wires' characteristics. Also, the bond length affected by wires slip was a little higher (165 mm, instead 150 mm). The -99D mesh provided a bit steeper performances, in respect to -66S, but very similar values for both the peak load and for the bond length affected by wire slip.

The orientation of the mesh was then varied by arranging the parallel fiber wires along the loading direction (-P). The tensile stress–strain curves [dashed lines in Fig. 16(a)] look generally stiffer and stronger when compared with the respective -T samples, due to the quite higher performances of the parallel fiber wires (Table 1); the crack pattern is almost the same. But, in the shear bond tests [Fig. 17(a)], the failure for yarns slippage occurred for all the investigated -P configurations, evidencing the necessity of a higher bond length to exploit the whole yarns resistance. This appears more clearly when analyzing the trend of the tangential forces along the wires [Fig. 17(b)], since in -P configurations the whole bond length was affected by slip at peak load ($v > 0$). It was also observed that a reduction or an increase

in the wires' tensile strength (e.g., ±35%) determines, respectively, a premature or postponed interruption of the capacity curves. Variations in the wires' Young's modulus affect the curve stiffness (in TS tests, only the third stage).

The effects due to variations of ±35% in the tensile strength of the mortar coating (suffix f_t), as well as in its thickness (suffix s), can be observed in Fig. 18(a), referring to tensile tests: basically, a stronger mortar matrix resulted in a higher cracking load, a more scattered cracking formation stage, and a more prominent tension–stiffening effect. The shear bond performances were not significantly influenced. The mortar Young's modulus has in general a negligible effect, for the investigated range (±35%), so the respective curves are not plotted. When scaling by ±35% the ordinates of the shear stress–slip relationship between the wires and the mortar matrix (L), a wider crack diffusion and a higher ultimate strains emerged at the increasing of the bond strength, in the tensile tests, and a reduction of the bond length affected by slip was detected in the shear bond tests [Fig. 18(b)]. The modified distribution of the tangential forces along the wires induced very few variations in the trends of the bond stresses along the mortar–masonry
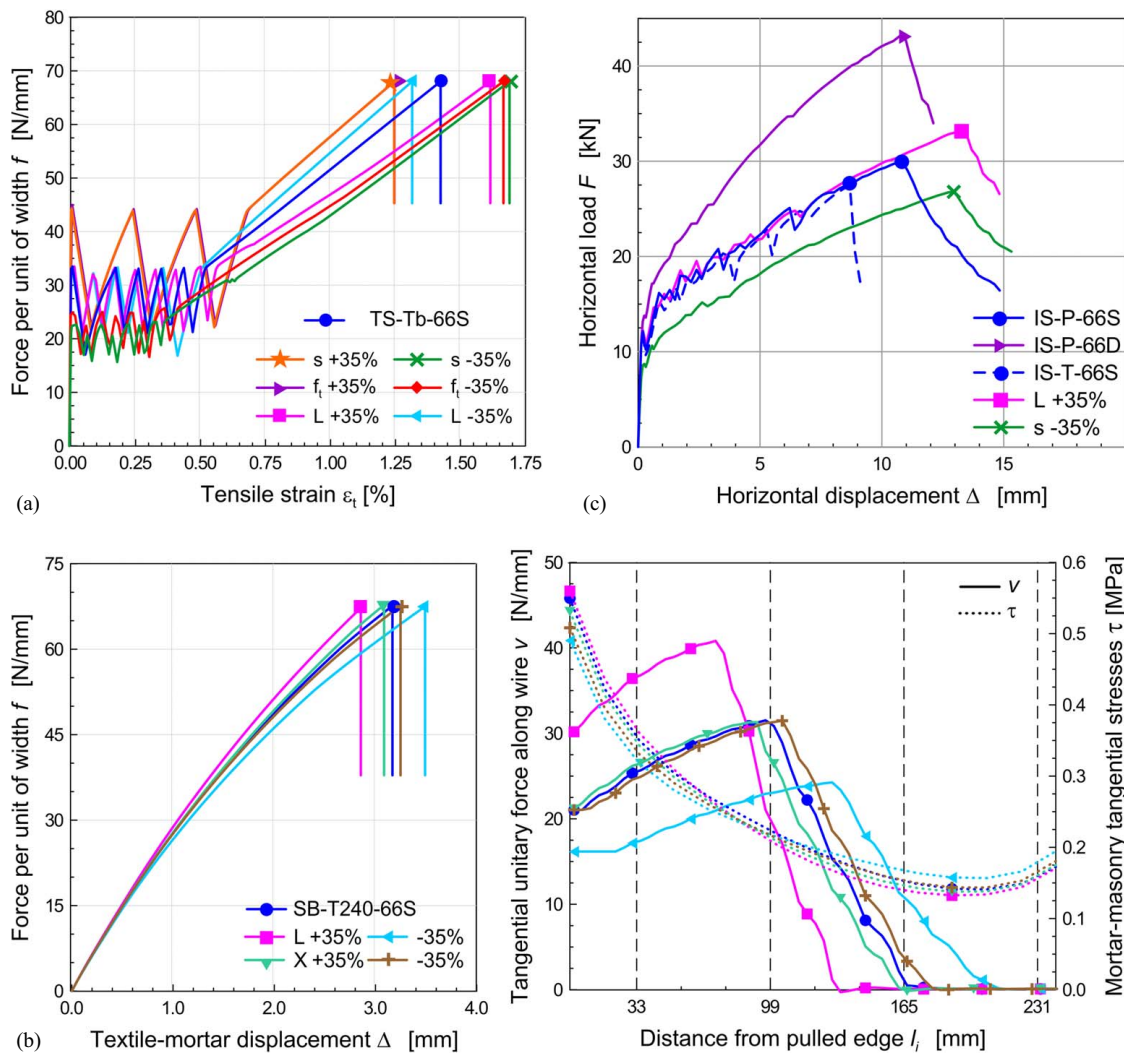
Fig. 18. Sensitivity analysis, with variations in the characteristics of the mortar and of the wires–mortar bond: (a) tensile tests; (b) shear bond test; and (c) in-plane shear tests.

interface, τ. Variations of $\pm 35\%$ in the resistance of the mesh intersections (X) had less influence, as expected, due to the lower contribution against the wires pullout from the coating, as already evidenced in the simulations of the pullout tests.

The sensitivity analysis performed on the in-plane shear setup [Fig. 18(c)] confirmed that the increase of the reinforcement ratio (e.g., -66D curve) can lead to stronger and stiffer performances. The reversion of the mesh orientation (-T sample) resulted in a lower resistance, according to the weaker performances of the wires arranged vertically, but the global stiffness was not affected. Reductions in the mortar thickness (as well as in the mortar tensile strength) decreased the ordinates and enlarged the ultimate displacement (S suffix). By increasing the wire–mortar bond strength (L), it was possible to avoid the collapse due to wires debonding at the base, improving the sample performances.

Conclusions

This paper collects the former results of a project aimed at the calibration of a numerical model for the prediction of the performances of historical masonry strengthened with TRM systems. The paper is focused, in particular, on the behavior of TRMs at the characterization test level.

In the first part, a broad literature review collects the main experimental tests features and points out the aspects influencing the response; in addition, the analytical and numerical models developed for the simulation of tensile and shear bond tests are described, evidencing the different assumptions. What emerges from the wide literature review is, on one hand, the large number of studies performed on a wide variety of TRM systems in a relatively short period (10–15 years), which testifies the interest in this topic and the great variety of features that deserve attention. But, on the other hand, it also emerges the clear lack of an exhaustive study on a specific TRM compound, comprehensive of the various aspects (at least, at the experimental level, let alone the numerical and analytical).

The second part of the paper deals with the calibration and validation of a detailed numerical model for TRM using free, open-source code. In the 3D model, the components (the reinforcement yarns, the mortar matrix, and, if present, the masonry support) were assembled by means of interface elements. The calibration of the characteristics of the materials and interfaces, with nonlinear behavior, was based on the results of experimental tests available in the literature. The model validation was achieved through comparison with the results of tensile, shear–bond, and in-plane shear experimental tests. The sensitivity of the models to the main components characteristics (reinforcement ratio and orientation,

mortar characteristics, wire–mortar interaction) was also investigated, with results confirming the evidence emerged from the state of the art. The parametric analyses also evidenced that the modest discrepancy emerged in the comparisons with the experimental results may be attributable to normal uncertainties and intrinsic scatter in the material and interface properties.

The detailed-level model herein applied for the calibration and validation of a CRM-strengthening technique has general validity and can also be applied on other TRM systems, once the appropriate characterization tests on materials and interfaces are performed. The model represents a useful tool to investigate on the TRM optimization, to calibrate applicative details and to define the equivalent behavior of TRM as homogenized material for simplified modeling purposes. The modeling method will be adopted for the simulation of in-plane and out-of-plane tests on masonry samples, to estimate the benefits and calibrate/validate simplified methods for the analysis of entire walls and buildings.

Data Availability Statement

Some or all data, models, or code generated or used during the study are available in a repository online in accordance with funder data retention policies (https://doi.org/10.5281/zenodo.5562187). OOFEM v.2.5 was used for running the analyses (Öhman et al. 2020).

Acknowledgments

References

ACI (American Concrete Institute). 2016. *Acceptance criteria for masonry and concrete strengthening using fabric-reinforced cementitious matrix (FRCM) and steel reinforced grout (SRG) composite systems*. AC 434. Naples, FL: ACI.

ACI (American Concrete Institute). 2020. *Guide to design and construction of externally bonded fabric-reinforced cementitious matrix (FRCM) and steel-reinforced grout (SRG) systems*. ACI 549.6R-20. Farmington Hills, MI: ACI.

Alecci, V., M. De Stefano, R. Luciano, L. Rovero, and G. Stipo. 2016. "Experimental investigation on bond behavior of cement-matrix–based composites for strengthening of masonry structures." *J. Compos. Constr.* 20 (1): 04015041. https://doi.org/10.1061/(ASCE)CC.1943-5614.0000598.

Al-Lami, K., T. D'Antino, and P. Colombi. 2020. "Durability of fabric-reinforced cementitious matrix (FRCM) composites: A review." *Appl. Sci.* 10 (5): 1714. https://doi.org/10.3390/app10051714.

Arboleda, D., S. Babaeidarabad, C. D. Hays, and A. Nanni. 2014. "Durability of fabric reinforced cementitious matrix (FRCM) composites." In *Proc., 7th Int. Conf. on FRP Composites in Civil Engineering*. Vancouver, Canada: International Institute for FRP in Construction.

Arboleda, D., F. G. Carozzi, A. Nanni, and C. Poggi. 2016. "Testing procedures for the uniaxial tensile characterization of fabric-reinforced cementitious matrix composites." *J. Compos. Constr.* 20 (3): 04015063. https://doi.org/10.1061/(ASCE)CC.1943-5614.0000626.

Ascione, F., M. Lamberti, A. Napoli, and R. Realfonzo. 2020. "Bond–slip models for the interface between steel fabric reinforced cementitious matrix and concrete substrate." *Composites, Part C: Open Access* 3: 100078. https://doi.org/10.1016/j.jcomc.2020.100078.

Ascione, L., G. de Felice, and S. De Santis. 2015. "A qualification method for externally bonded fibre reinforced cementitious matrix (FRCM) strengthening systems." *Composites, Part B* 78: 497–506. https://doi.org/10.1016/j.compositesb.2015.03.079.

Askouni, P. D., and C. G. Papanicolaou. 2017. "Experimental investigation of bond between glass textile reinforced mortar overlays and masonry: The effect of bond length." *Mater. Struct.* 50 (2): 164. https://doi.org/10.1617/s11527-017-1033-7.

Askouni, P. D., and C. G. Papanicolaou. 2019. "Textile reinforced mortar-to-masonry bond: Experimental investigation of bond-critical parameters." *Constr. Build. Mater.* 207: 535–547. https://doi.org/10.1016/j.conbuildmat.2019.02.102.

Aveston, J., and A. Kelly. 1973. "Theory of multiple fracture of fibrous composites." *J. Mater. Sci.* 8 (3): 352–362. https://doi.org/10.1007/BF00550155.

Barattucci, S., V. Sarhosis, A. W. Bruno, A. M. D'Altri, S. de Miranda, and G. Castellazzi. 2020. "An experimental and numerical study on masonry triplets subjected to monotonic and cyclic shear loadings." *Constr. Build. Mater.* 254: 119313. https://doi.org/10.1016/j.conbuildmat.2020.119313.

Barducci, S., V. Alecci, M. De Stefano, G. Misseri, L. Rovero, and G. Stipo. 2020. "Experimental and analytical investigations on bond behavior of basalt-FRCM systems." *J. Compos. Constr.* 24 (1): 04019055. https://doi.org/10.1061/(ASCE)CC.1943-5614.0000985.

Basset-Salom, L., and A. Guardiola-Víllora. 2014. "Seismic performance of masonry residential buildings in Lorca's city centre, after the 11th May 2011 earthquake." *Bull. Earthquake Eng.* 12 (5): 2027–2048. https://doi.org/10.1007/s10518-013-9559-8.

Bellini, A., and C. Mazzotti. 2016. "Bond behavior and tensile properties of FRCM composites applied on masonry panels." In *Structural analysis of historical constructions: Anamnesis, diagnosis, therapy, controls*, edited by K. Van Balen and E. Verstrynge. London. Taylor & Francis Group.

Bellini, A., S. K. Shahreza, and C. Mazzotti. 2019. "Cyclic bond behavior of FRCM composites applied on masonry substrate." *Composites, Part B* 169: 189–199. https://doi.org/10.1016/j.compositesb.2019.04.009.

Bertolesi, E., F. G. Carozzi, G. Milani, and C. Poggi. 2014. "Numerical modeling of fabric reinforce cementitious matrix composites (FRCM) in tension." *Constr. Build. Mater.* 70: 531–548. https://doi.org/10.1016/j.conbuildmat.2014.08.006.

Bertolesi, E., E. Grande, and G. Milani. 2019. "Numerical modeling of the bond behaviour of FRCM systems externally applied to masonry substrates." *J. Build. Pathol. Rehabil.* 4: 4. https://doi.org/10.1007/s41024-019-0046-8.

Bilotta, A., F. Ceroni, E. Nigro, and M. Pecce. 2017. "Experimental tests on FRCM strengthening systems for tuff masonry elements." *Constr. Build. Mater.* 138: 114–133. https://doi.org/10.1016/j.conbuildmat.2017.01.124.

Binda, L., A. Anzani, and A. Saisi. 2003. "1.02 - Historic masonry structures." In *Comprehensive structural integrity*, edited by I. Milne, R. O. Ritchie, and B. Karihaloo, 25–47. Oxford, UK: Pergamon.

Boem, I. 2021a. https://sites.google.com/view/confirmaproject.

Boem, I. 2021b. "ConFiRMa dataset_01: simulation of CRM characterization tests with the OOFEM code (detailed level modelling) (v.01.1)." Accessed April 11, 2022. https://doi.org/10.5281/zenodo.6448372.

Butler, M., V. Mechtcherine, and S. Hempel. 2009. "Experimental investigations on the durability of fiber–matrix interfaces in textile-reinforced concrete." *Cem. Concr. Compos.* 31 (4): 221–231. https://doi.org/10.1016/j.cemconcomp.2009.02.005.

Butler, M., V. Mechtcherine, and S. Hempel. 2010. "Durability of textile reinforced concrete made with AR glass fiber: Effect of the matrix composition." *Mater. Struct.* 43 (10): 1351–1368. https://doi.org/10.1617/s11527-010-9586-8.

Caggegi, C., F. G. Carozzi, S. De Santis, F. Fabbrocino, F. Focacci, Ł. Hojdys, E. Lanoye, and L. Zuccarino. 2017. "Experimental analysis on tensile and bond properties of PBO and aramid fabric reinforced cementitious matrix for strengthening masonry structures." *Composites, Part B* 127: 175–195. https://doi.org/10.1016/j.compositesb.2017.05.048.

Calabrese, A. S., P. Colombi, and T. D'Antino. 2019. "Analytical solution of the bond behavior of FRCM composites using a rigid-softening cohesive material law." *Composites, Part B* 174: 107051. https://doi.org/10.1016/j.compositesb.2019.107051.

Calabrese, A. S., T. D'Antino, P. Colombi, and C. Poggi. 2020. "Study of the influence of interface normal stresses on the bond behavior of FRCM composites using direct shear and modified beam tests." *Constr. Build. Mater.* 262: 120029. https://doi.org/10.1016/j.conbuildmat.2020.120029.

Calderini, C., and S. Lagomarsino. 2008. "Continuum model for in-plane anisotropic inelastic behavior of masonry." *J. Struct. Eng.* 134 (2): 209–220. https://doi.org/10.1061/(ASCE)0733-9445(2008)134:2(209).

Carloni, C., T. D'Antino, L. H. Sneed, and C. Pellegrino. 2018. "Three-dimensional numerical modeling of single-lap direct shear tests of FRCM-concrete joints using a cohesive damaged contact approach." *J. Compos. Constr.* 22 (1): 04017048. https://doi.org/10.1061/(ASCE)CC.1943-5614.0000827.

Carozzi, F. G., P. Colombi, G. Fava, and C. Poggi. 2016. "A cohesive interface crack model for the matrix–textile debonding in FRCM composites." *Compos. Struct.* 143: 230–241. https://doi.org/10.1016/j.compstruct.2016.02.019.

Carozzi, F. G., G. Milani, and C. Poggi. 2014. "Mechanical properties and numerical modeling of fabric reinforced cementitious matrix (FRCM) systems for strengthening of masonry structures." *Compos. Struct.* 107: 711–725. https://doi.org/10.1016/j.compstruct.2013.08.026.

Carozzi, F. G., and C. Poggi. 2015. "Mechanical properties and debonding strength of fabric reinforced cementitious matrix (FRCM) systems for masonry strengthening." *Composites, Part B* 70: 215–230. https://doi.org/10.1016/j.compositesb.2014.10.056.

Carozzi, F. G., et al. 2017. "Experimental investigation of tensile and bond properties of carbon-FRCM composites for strengthening masonry elements." *Composites, Part B* 128: 100–119. https://doi.org/10.1016/j.compositesb.2017.06.018.

CEB (Comité Euro-International du Béton). 2010. *Model code 2010*. Paris: FIP.

CEN (Comité Européen de Normalisation). 2004. *Design of concrete structures - Part 1-1: General rules and rules for buildings*. EN 1992-1-1:2004, Eurocode 2. Brussels, Belgium: CEN.

CEN (Comité Européen de Normalisation). 2009. *Testing hardened concrete - Part 6: Tensile splitting strength of test specimens*. EN 12390-6:2009. Brussels, Belgium: CEN.

CEN (Comité Européen de Normalisation). 2019a. *Steel for the reinforcement and prestressing of concrete - Test methods - Part 2: Welded fabric and lattice girders*. EN ISO 15630-2:2019. Brussels, Belgium: CEN.

CEN (Comité Européen de Normalisation). 2019b. *Testing hardened concrete - Part 3: Compressive strength of test specimens*. EN 12390-3:2019. Brussels, Belgium: CEN.

CEN (Comité Européen de Normalisation). 2021. *Testing hardened concrete - Part 13: Determination of secant modulus of elasticity in compression*. EN 12390-13:2021. Brussels, Belgium: CEN.

CNR (Consiglio Nazionale delle Ricerche). 2020. *Guide for the design and construction of externally bonded fibre reinforced inorganic matrix systems for strengthening existing structure*. CNR-DT 215/2018, rev. June 2020. Rome: CNR.

Colombi, P., and T. D'Antino. 2019. "Analytical assessment of the stress-transfer mechanism in FRCM composites." *Compos. Struct.* 220: 961–970. https://doi.org/10.1016/j.compstruct.2019.03.074.

Colombo, I., M. Colombo, A. Magri, G. Zani, and M. di Prisco. 2011. "Textile reinforced mortar at high temperatures." *Appl. Mech. Mater.* 82: 202–207. https://doi.org/10.4028/www.scientific.net/AMM.82.202.

Contamine, R., A. Si Larbi, and P. Hamelin. 2011. "Contribution to direct tensile testing of textile reinforced concrete (TRC) composites." *Mater. Sci. Eng. A* 528 (29–30): 8589–8598. https://doi.org/10.1016/j.msea.2011.08.009.

Cosenza, E., G. Manfredi, and R. Realfonzo. 1997. "Behavior and modeling of bond of FRP rebars to concrete." *J. Compos. Constr.* 1 (2): 40–51. https://doi.org/10.1061/(ASCE)1090-0268(1997)1:2(40).

CSLP (Consiglio Superiore del Lavori Pubblici). 2018. *Guideline for the identification, qualification and acceptance control of fibre reinforced cementitious matrix (FRCM) used for the structural consolidation of existing constructions*. [In Italian]. CSLP 01/01/2019, n.1. Rome: CSLP.

CSLP (Consiglio Superiore del Lavori Pubblici). 2019a. *Guidelines for design, execution and maintenance of strengthening interventions by means of fibre reinforced cementitious matrix (FRCM) systems*. [In Italian]. CSLP 03/12/2019, n. 627. Rome: CSLP.

CSLP (Consiglio Superiore del Lavori Pubblici). 2019b. *Guideline for the identification, qualification and acceptance control of fiber-reinforced composites systems with preformed mesh, based on polymer matrix, used for the structural consolidation of existing constructions with the CRM (composite reinforced mortar) technique*. [In Italian]. CSLP 29/05/2019, n. 292. Rome: CSLP.

Dalalbashi, A., B. Ghiassi, D. V. Oliveira, and A. Freitas. 2018a. "Effect of test setup on the fiber-to-mortar pullout response in TRM composites: Experimental and analytical modeling." *Composites, Part B* 143: 250–268. https://doi.org/10.1016/j.compositesb.2018.02.010.

Dalalbashi, A., B. Ghiassi, D. V. Oliveira, and A. Freitas. 2018b. "Fiber-to-mortar bond behavior in TRM composites: Effect of embedded length and fiber configuration." *Composites, Part B* 152: 43–57. https://doi.org/10.1016/j.compositesb.2018.06.014.

D'Ambrisi, A., L. Feo, and F. Focacci. 2013. "Experimental and analytical investigation on bond between carbon-FRCM materials and masonry." *Composites, Part B* 46: 15–20. https://doi.org/10.1016/j.compositesb.2012.10.018.

D'Antino, T., C. Carloni, L. H. Sneed, and C. Pellegrino. 2014. "Matrix–fiber bond behavior in PBO FRCM composites: A fracture mechanics approach." *Eng. Fract. Mech.* 117: 94–111. https://doi.org/10.1016/j.engfracmech.2014.01.011.

D'Antino, T., P. Colombi, C. Carloni, and L. H. Sneed. 2018. "Estimation of a matrix–fiber interface cohesive material law in FRCM-concrete joints." *Compos. Struct.* 193: 103–112. https://doi.org/10.1016/j.compstruct.2018.03.005.

D'Antino, T., and C. Papanicolaou. 2017. "Mechanical characterization of textile reinforced inorganic-matrix composites." *Composites, Part B* 127: 78–91. https://doi.org/10.1016/j.compositesb.2017.02.034.

D'Antino, T., and C. Papanicolaou. 2018. "Comparison between different tensile test set-ups for the mechanical characterization of inorganic-matrix composites." *Constr. Build. Mater.* 171: 140–151. https://doi.org/10.1016/j.conbuildmat.2018.03.041.

de Carvalho Bello, C. B., I. Boem, A. Cecchi, N. Gattesco, and D. V. Oliveira. 2019. "Experimental tests for the characterization of sisal fiber reinforced cementitious matrix for strengthening masonry structures." *Constr. Build. Mater.* 219: 44–55. https://doi.org/10.1016/j.conbuildmat.2019.05.168.

de Felice, G., S. De Santis, L. Garmendia, B. Ghiassi, P. Larrinaga, P. B. Lourenço, D. V. Oliveira, F. Paolacci, and C. G. Papanicolaou. 2014. "Mortar-based systems for externally bonded strengthening of masonry." *Mater. Struct.* 47 (12): 2021–2037. https://doi.org/10.1617/s11527-014-0360-1.

De Santis, S., F. G. Carozzi, G. de Felice, and C. Poggi. 2017b. "Test methods for textile reinforced mortar systems." *Composites, Part B* 127: 121–132. https://doi.org/10.1016/j.compositesb.2017.03.016.

De Santis, S., and G. de Felice. 2015. "Tensile behaviour of mortar-based composites for externally bonded reinforcement systems." *Composites, Part B* 68: 401–413. https://doi.org/10.1016/j.compositesb.2014.09.011.

De Santis, S., et al. 2017a. "Round robin test on tensile and bond behaviour of steel reinforced grout systems." *Composites, Part B* 127: 100–120. https://doi.org/10.1016/j.compositesb.2017.03.052.

Donnini, J. 2019. "Durability of glass FRCM systems: Effects of different environments on mechanical properties." *Composites, Part B* 174: 107047. https://doi.org/10.1016/j.compositesb.2019.107047.

Donnini, J., F. De Caso y Basalo, V. Corinaldesi, G. Lancioni, and A. Nanni. 2017. "Fabric-reinforced cementitious matrix behavior at high-temperature: Experimental and numerical results." *Compos. Part B Eng.* 108: 108–121. https://doi.org/10.1016/j.compositesb.2016.10.004.

Donnini, J., and V. Corinaldesi. 2017. "Mechanical characterization of different FRCM systems for structural reinforcement." *Constr. Build. Mater.* 145: 565–575. https://doi.org/10.1016/j.conbuildmat.2017.04.051.

Donnini, J., V. Corinaldesi, and A. Nanni. 2016. "Mechanical properties of FRCM using carbon fabrics with different coating treatments." *Composites, Part B* 88: 220–228. https://doi.org/10.1016/j.compositesb.2015.11.012.

Donnini, J., G. Lancioni, and V. Corinaldesi. 2018. "Failure modes in FRCM systems with dry and pre-impregnated carbon yarns: Experiments and modeling." *Composites, Part B* 140: 57–67. https://doi.org/10.1016/j.compositesb.2017.12.024.

Dvorkin, D., A. Poursaee, A. Peled, and W. J. Weiss. 2013. "Influence of bundle coating on the tensile behavior, bonding, cracking and fluid transport of fabric cement-based composites." *Cem. Concr. Compos.* 42: 9–19. https://doi.org/10.1016/j.cemconcomp.2013.05.005.

Fernandes, F., P. B. Lourenço, and F. Castro. 2010. "Ancient clay bricks: Manufacture and properties." In *Materials, technologies and practice in historic heritage structures*, edited by M. B. Dan, R. Přikryl, and Á Török. Dordrecht, Netherlands: Springer.

Fiorentino, G., A. Forte, E. Pagano, F. Sabetta, C. Baggio, D. Lavorato, C. Nuti, and S. Santini. 2018. "Damage patterns in the town of Amatrice after August 24th 2016 Central Italy earthquakes." *Bull. Earthquake Eng.* 16 (3): 1399–1423. https://doi.org/10.1007/s10518-017-0254-z.

Focacci, F., T. D'Antino, and C. Carloni. 2020. "The role of the fiber–matrix interfacial properties on the tensile behavior of FRCM coupons." *Constr. Build. Mater.* 265: 120263. https://doi.org/10.1016/j.conbuildmat.2020.120263.

Focacci, F., T. D'Antino, C. Carloni, L. H. Sneed, and C. Pellegrino. 2017. "An indirect method to calibrate the interfacial cohesive material law for FRCM-concrete joints." *Mater. Des.* 128: 206–217. https://doi.org/10.1016/j.matdes.2017.04.038.

Gattesco, N., and I. Boem. 2015. "Experimental and analytical study to evaluate the effectiveness of an in-plane reinforcement for masonry walls using GFRP meshes." *Constr. Build. Mater.* 88: 94–104. https://doi.org/10.1016/j.conbuildmat.2015.04.014.

Gattesco, N., and I. Boem. 2017a. "Characterization tests of GFRM coating as a strengthening technique for masonry buildings." *Compos. Struct.* 165: 209–222. https://doi.org/10.1016/j.compstruct.2017.01.043.

Gattesco, N., and I. Boem. 2017b. "Out-of-plane behavior of reinforced masonry walls: Experimental and numerical study." *Composites, Part B* 128: 39–52. https://doi.org/10.1016/j.compositesb.2017.07.006.

Ghiassi, B., D. V. Oliveira, V. Marques, E. Soares, and H. Maljaee. 2016. "Multi-level characterization of steel reinforced mortars for strengthening of masonry structures." *Mater. Des.* 110: 903–913. https://doi.org/10.1016/j.matdes.2016.08.034.

Gostič, S., and B. Dolinšek. 2008. "Lessons learned after 1998 and 2004 earthquake in Posočje region." In *Proc. 4th Int i-Rec Conf. Building Resilience: Achieving Effective Post-Disaster Reconstruction*, edited by D. Myburgh, E. Seville, and S. Wilkinson. Christchurch, New Zealand: University of Canterbury.

Grande, E., M. Imbimbo, and E. Sacco. 2013. "Modeling and numerical analysis of the bond behavior of masonry elements strengthened with SRP/SRG." *Composites, Part B* 55: 128–138. https://doi.org/10.1016/j.compositesb.2013.06.003.

Grande, E., M. Imbimbo, and E. Sacco. 2018. "Numerical investigation on the bond behavior of FRCM strengthening systems." *Composites, Part B* 145: 240–251. https://doi.org/10.1016/j.compositesb.2018.03.010.

Grande, E., and G. Milani. 2018. "Interface modeling approach for the study of the bond behavior of FRCM strengthening systems." *Composites, Part B* 141: 221–233. https://doi.org/10.1016/j.compositesb.2017.12.052.

Grande, E., G. Milani, and M. Imbimbo. 2020. "Theoretical model for the study of the tensile behavior of FRCM reinforcements." *Constr. Build. Mater.* 236: 117617. https://doi.org/10.1016/j.conbuildmat.2019.117617.

Grassl, P., and M. Jirásek. 2006. "Damage-plastic model for concrete failure." *Int. J. Solids Struct.* 43 (22–23): 7166–7196. https://doi.org/10.1016/j.ijsolstr.2006.06.032.

Hadad, H., D. Campanini, and A. Nanni. 2021. *Effect of bonded length on material characterization of FRCM composites*. ACI Symposium Publication 345. Farmington Hills, MI: ACI.

Kim, H.-S., G. T. Truong, S.-H. Park, and K. K. Choi. 2018. "Tensile properties of carbon fiber-textile reinforced mortar (TRM) characterized by different anchorage methods." *Int. J. Concr. Struct. Mater.* 12 (1): 73. https://doi.org/10.1186/s40069-018-0296-x.

Kouris, L. A. S., and T. C. Triantafillou. 2018. "State-of-the-art on strengthening of masonry structures with textile reinforced mortar (TRM)." *Constr. Build. Mater.* 188: 1221–1233. https://doi.org/10.1016/j.conbuildmat.2018.08.039.

Larrinaga, P., C. Chastre, H. C. Biscaia, and J. T. San-José. 2014. "Experimental and numerical modeling of basalt textile reinforced mortar behavior under uniaxial tensile stress." *Mater. Des.* 55: 66–74. https://doi.org/10.1016/j.matdes.2013.09.050.

Larrinaga, P., C. Chastre, J. T. San-José, and L. Garmendia. 2013. "Non-linear analytical model of composites based on basalt textile reinforced mortar under uniaxial tension." *Composites, Part B* 55: 518–527. https://doi.org/10.1016/j.compositesb.2013.06.043.

Leone, M., et al. 2017. "Glass fabric reinforced cementitious matrix: Tensile properties and bond performance on masonry substrate." *Composites, Part B* 127: 196–214. https://doi.org/10.1016/j.compositesb.2017.06.028.

Lignola, G. P., et al. 2017. "Performance assessment of basalt FRCM for retrofit applications on masonry." *Composites, Part B* 128: 1–18. https://doi.org/10.1016/j.compositesb.2017.05.003.

Lin, Q., X. Xue, Z. Guo, Y. Zhao, and Y. Chen. 2021. "Test on shear behavior of less-tightened high-strength bolted connections." *Structures* 34: 3622–3639. https://doi.org/10.1016/j.istruc.2021.09.104.

Liu, S., X. Wang, P. Rawat, Z. Chen, C. Shi, and D. Zhu. 2021. "Experimental study and analytical modeling on tensile performance of basalt textile reinforced concrete." *Constr. Build. Mater.* 267: 120972. https://doi.org/10.1016/j.conbuildmat.2020.120972.

Liu, S., D. Zhu, X. Wang, and C. Shi. 2019. "Pullout properties of AR-glass textile embedded in cement matrix under different velocities and temperatures." *Constr. Build. Mater.* 228: 116779. https://doi.org/10.1016/j.conbuildmat.2019.116779.

Lourenço, P. B., and J. G. Rots. 1997. "Multisurface interface model for analysis of masonry structures." *J. Eng. Mech.* 123 (7): 660–668. https://doi.org/10.1061/(ASCE)0733-9399(1997)123:7(660).

Macorini, L., and B. A. Izzuddin. 2013. "Nonlinear analysis of masonry structures using mesoscale partitioned modelling." *Adv. Eng. Software* 60–61: 58–69. https://doi.org/10.1016/j.advengsoft.2012.11.008.

Magenes, G. 2000. "A method for pushover analysis in seismic assessment of masonry buildings." In *Proc XII World Conf. on Earthquake Engineering*. Auckland, NZ: New Zealand Society for Earthquake Engineering.

Makovička, D., and D. Makovička, Jr. 2003. "Explosive failuring of masonry structure." In *Transactions of the 17th Int. Conf. on Structural Mechanics in Reactor Technology*, paper #J04-2. Prague, Czech Republic: International Association for Structural Mechanics in Reactor Technology SMiRT.

Martins, A., G. Vasconcelos, R. Fangueiro, and F. Cunha. 2015. "Experimental assessment of an innovative strengthening material for brick masonry infills." *Composites, Part B* 80: 328–342. https://doi.org/10.1016/j.compositesb.2015.06.012.

Micelli, F., and M. A. Aiello. 2019. "Residual tensile strength of dry and impregnated reinforcement fibers after exposure to alkaline environments." *Composites, Part B* 159: 490–501. https://doi.org/10.1016/j.compositesb.2017.03.005.

Micelli, F., et al. 2017. "Experimental investigation of tensile and bond properties of carbon-FRCM composites for strengthening masonry elements." *Composites, Part B* 128: 100–119. https://doi.org/10.1016/j.compositesb.2017.06.018.

Nerilli, F., S. Marfia, and E. Sacco. 2020. "Micromechanical modeling of the constitutive response of FRCM composites." *Constr. Build. Mater.* 236: 117539. https://doi.org/10.1016/j.conbuildmat.2019.117539.

Nobili, A. 2016. "Durability assessment of impregnated glass fabric reinforced cementitious matrix (GFRCM) composites in the alkaline and saline environments." *Constr. Build. Mater.* 105: 465–471. https://doi.org/10.1016/j.conbuildmat.2015.12.173.

Nobili, A., and C. Signorini. 2017. "On the effect of curing time and environmental exposure on impregnated carbon fabric reinforced cementitious matrix (CFRCM) composite with design considerations." *Composites, Part B* 112: 300–313. https://doi.org/10.1016/j.compositesb.2016.12.022.

Öhman, M., et al. 2020. "Oofem/oofem: OOFEM, version 2.5 (v2.5)." Accessed November 18, 2021. https://doi.org/10.5281/zenodo.4339630.

Olivito, R. S., R. Codispoti, and O. A. Cevallos. 2016. "Bond behavior of flax-FRCM and PBO-FRCM composites applied on clay bricks: Experimental and theoretical study." *Compos. Struct.* 146: 221–231. https://doi.org/10.1016/j.compstruct.2016.03.004.

Padalu, P. K. V. R., Y. Singh, and S. Das. 2018. "Efficacy of basalt fiber reinforced cement mortar composite for out-of-plane strengthening of unreinforced masonry." *Constr. Build. Mater.* 191: 1172–1190. https://doi.org/10.1016/j.conbuildmat.2018.10.077.

Papanicolaou, C. G., T. C. Triantafillou, K. Karlos, and M. Papathanasiou. 2007a. "Textile-reinforced mortar (TRM) versus FRP as strengthening material of URM walls: In-plane cyclic loading." *Mater. Struct.* 40 (10): 1081–1097. https://doi.org/10.1617/s11527-006-9207-8.

Papanicolaou, C. G., T. C. Triantafillou, M. Papathanasiou, and K. Karlos. 2007b. "Textile reinforced mortar (TRM) versus FRP as strengthening material of URM walls: Out-of-plane cyclic loading." *Mater. Struct.* 41 (1): 143–157. https://doi.org/10.1617/s11527-007-9226-0.

Patzák, B. 2002. http://www.oofem.org.

Patzák, B. 2012. "OOFEM — An object-oriented simulation tool for advanced modeling of materials and structures." *Acta Polytech.* 52 (6): 59–66. https://doi.org/10.14311/1678.

Patzák, B., and Z. Bittnar. 2001. "Design of object oriented finite element code." *Adv. Eng. Software* 32 (10–11): 759–767. https://doi.org/10.1016/S0965-9978(01)00027-8.

Peled, A., and A. Bentur. 2003. "Fabric structure and its reinforcing efficiency in textile reinforced cement composites." *Composites, Part A* 34 (2): 107–118. https://doi.org/10.1016/S1359-835X(03)00003-4.

Penna, A., P. Morandi, M. Rota, C. F. Manzini, F. da Porto, and G. Magenes. 2014. "Performance of masonry buildings during the Emilia 2012 earthquake." *Bull. Earthquake Eng.* 12 (5): 2255–2273. https://doi.org/10.1007/s10518-013-9496-6.

Razavizadeh, A., B. Ghiassi, and D. V. Oliveira. 2014. "Bond behavior of SRG-strengthened masonry units: Testing and numerical modeling." *Constr. Build. Mater.* 64: 387–397. https://doi.org/10.1016/j.conbuildmat.2014.04.070.

Righetti, L., M. Corradi, A. Borri, G. Castori, R. Sisti, and A. I. Osofero. 2016. "Durability of GFRP grids for masonry structures." *Int. J. Forensic Eng.* 3 (1/2): 164–179. https://doi.org/10.1504/IJFE.2016.075990.

Rovero, L., S. Galassi, and G. Misseri. 2020. "Experimental and analytical investigation of bond behavior in glass fiber-reinforced composites based on gypsum and cement matrices." *Composites, Part B* 194: 108051. https://doi.org/10.1016/j.compositesb.2020.108051.

Santandrea, M., F. Focacci, C. Mazzotti, F. Ubertini, and C. Carloni. 2020. "Determination of the interfacial cohesive material law for SRG composites bonded to a masonry substrate." *Eng. Fail. Anal.* 111: 104322. https://doi.org/10.1016/j.engfailanal.2019.104322.

Senaldi, I. E., G. Guerrini, A. Bruggi, A. Penna, and M. Quaini. 2020. "Experimental characterization of PBO-FRCM composites for masonry structures retrofit." In *Brick and block masonry - From historical to sustainable*, edited by J. Kubica, A. Kwiecień, and Ł Bednarz. London. Taylor & Francis.

Signorini, C., A. Nobili, E. I. Cedillo González, and C. Siligardi. 2018a. "Silica coating for interphase bond enhancement of carbon and AR-glass textile reinforced mortar (TRM)." *Composites, Part B* 141: 191–202. https://doi.org/10.1016/j.compositesb.2017.12.045.

Signorini, C., A. Nobili, and F. O. Falope. 2018b. "Mechanical performance and crack pattern analysis of aged carbon fabric cementitious matrix (CFRCM) composites." *Compos. Struct.* 202: 1114–1120. https://doi.org/10.1016/j.compstruct.2018.05.052.

Silva, F. de A., M. Butler, S. Hempel, R. D. Toledo Filho, and V. Mechtcherine. 2014. "Effects of elevated temperatures on the interface properties of carbon textile-reinforced concrete." *Cem. Concr. Compos.* 48: 26–34. https://doi.org/10.1016/j.cemconcomp.2014.01.007.

Sisti, R., G. Castori, A. Dudine, and A. Borri. 2019. "In-plane response of mortar plates strengthened by traditional or innovative reinforcement materials." [In Italian]. In *Proc XVIII Conference "ANIDIS L'ingegneria Sismica in Italia"*. Ascoli Piceno, Italy: Pisa University Press.

Sorrentino, L., S. Cattari, F. da Porto, G. Magenes, and A. Penna. 2019. "Seismic behaviour of ordinary masonry buildings during the 2016 central Italy earthquakes." *Bull. Earthquake Eng.* 17 (10): 5583–5607. https://doi.org/10.1007/s10518-018-0370-4.

Tamborrino, O., D. Perrone, and M. Leone. 2021. "Numerical modelling of shear bond tests on externally strengthened masonry specimens." In *Proc., 8th Int. Conf. on Computational Methods in Structural Dynamics and Earthquake Engineering*, edited by M. Papadrakakis, and M. Fragiadakis. London: International Society for Soil Mechanics and Geotechnical Engineering.

Tomaževič, M. 1999. *Earthquake-Resistant design of masonry buildings*. Series on innovation in structures and construction. London: Imperial College Press.

Tran, H. V., G. T. Truong, and K.-K. Choi. 2019. "Effect of harsh conditions on the tensile behaviour of lap-spliced carbon fiber textile-reinforced mortar (TRM) with different surface treatment methods." *Appl. Sci.* 9 (15): 3087. https://doi.org/10.3390/app9153087.

Trochoutsou, N., M. Di Benedetti, K. Pilakoutas, and M. Guadagnini. 2021. "Mechanical characterisation of flax and jute textile-reinforced mortars." *Constr. Build. Mater.* 271: 121564. https://doi.org/10.1016/j.conbuildmat.2020.121564.

Ural, A., A. Doğangün, H. Sezen, and Z. Angın. 2012. "Seismic performance of masonry buildings during the 2007 Bala, Turkey earthquakes." *Nat. Hazard.* 60 (3): 1013–1026. https://doi.org/10.1007/s11069-011-9887-4.

Van der Pluijm, R., H. Rutten, and M. Ceelen. 2000. "Shear behaviour of bed joints." In *Proc., 12th Int. Brick/Block Masonry Conf.*, edited by J. M. Adell. Madrid, Spain: IBMaC.

Wilson, M. P., G. R. Foulger, J. G. Gluyas, R. J. Davies, and B. R. Julian. 2017. "HiQuake: The human-induced earthquake database." *Seismol. Res. Lett.* 88 (6): 1560–1565. https://doi.org/10.1785/0220170112.

Zhang, S., N. Richart, and K. Beyer. 2018. "Numerical evaluation of test setups for determining the shear strength of masonry." *Mater. Struct.* 51 (4): 110. https://doi.org/10.1617/s11527-018-1236-6.

Zhu, D., A. Peled, and B. Mobasher. 2011. "Dynamic tensile testing of fabric–cement composites." *Constr. Build. Mater.* 25 (1): 385–395. https://doi.org/10.1016/j.conbuildmat.2010.06.014.